

Aeroacoustic Benchmarking of Trailing-Edge Noise from NACA 63₃ -018 Airfoil with Trailing-Edge Serrations

Luesutthiviboon, Salil; Pereira, Lourenço Tércio Lima; Ragni, Daniele; Avallone, Francesco; Snellen, Mirjam

DOI

[10.2514/1.J061630](https://doi.org/10.2514/1.J061630)

Publication date

2023

Document Version

Final published version

Published in

AIAA Journal

Citation (APA)

Luesutthiviboon, S., Pereira, L. T. L., Ragni, D., Avallone, F., & Snellen, M. (2023). Aeroacoustic Benchmarking of Trailing-Edge Noise from NACA 63₃ -018 Airfoil with Trailing-Edge Serrations. *AIAA Journal*, 61(1), 329-354. <https://doi.org/10.2514/1.J061630>

Important note

To cite this publication, please use the final published version (if applicable).
Please check the document version above.

Copyright

Other than for strictly personal use, it is not permitted to download, forward or distribute the text or part of it, without the consent of the author(s) and/or copyright holder(s), unless the work is under an open content license such as Creative Commons.

Takedown policy

Please contact us and provide details if you believe this document breaches copyrights.
We will remove access to the work immediately and investigate your claim.

Green Open Access added to TU Delft Institutional Repository

'You share, we take care!' - Taverne project

<https://www.openaccess.nl/en/you-share-we-take-care>

Otherwise as indicated in the copyright section: the publisher is the copyright holder of this work and the author uses the Dutch legislation to make this work public.

Aeroacoustic Benchmarking of Trailing-Edge Noise from NACA 63₃–018 Airfoil with Trailing-Edge Serrations

Salil Luesutthiviboon,^{*} Lourenço Tércio Lima Pereira,[†] Daniele Ragni,[‡] Francesco Avallone,[§] and Mirjam Snellen[¶]

Delft University of Technology, 2629 HS Delft, The Netherlands

<https://doi.org/10.2514/1.J061630>

Experimental results on trailing-edge (TE) noise from a NACA 63₃–018 airfoil are presented for a chord-based Reynolds number Re_c range between 2×10^5 and 3×10^6 . Far-field TE noise from the baseline airfoil with a straight TE and TE serrations is measured with varying Re_c , angle of attack, and serration shape and flap angle. Additionally, aerodynamic coefficients and boundary-layer parameters at the TE are also reported. To cover such a broad Re_c range, two NACA 63₃–018 airfoil models were tested in two different wind tunnels. The measurements include the emitted noise with natural and forced transition locations. For the straight TE, the forced transition location results in up to 5 dB increase of the far-field TE noise level, compared to the natural one. Scaling of the far-field noise spectra from the baseline TE shows that the Strouhal numbers St at which the peak noise level is measured reduce as Re_c increases. TE noise spectra for the cases with the TE serrations are found to be dependent on the airfoil lift and Re_c . The present data are to be included in the framework of the Benchmark Problems for Airframe Noise Computations category I and are publicly available in a repository with the following digital object identifier (DOI): <https://doi.org/10.4121/20940646>.

Nomenclature

b	=	span, m
C	=	Coles' fitting coefficient
c	=	chord, m
c_d	=	drag coefficient
c_l	=	lift coefficient
c_p	=	pressure coefficient
f	=	frequency, Hz
H	=	shape factor
h	=	serrations amplitude, m
K_B	=	Brooks's angle correction factor
K_{TL}	=	transmission loss empirical coefficient
$K_{\delta_{99}}$	=	boundary-layer thickness factor
L_A	=	A-weighted overall sound pressure level, dB(A)
M	=	Mach number
\hat{n}_a	=	unit vector in direction of a
p_s	=	static pressure, Pa
p_t	=	total pressure, Pa
Re_a	=	Reynolds number based on a
St_a	=	Strouhal number based on a
s	=	direction along airfoil surface
t_{TE}	=	trailing-edge thickness, m
u	=	flow velocity, m/s
u_e	=	edge velocity, m/s
u_τ	=	friction velocity, m/s
X	=	streamwise distance, m
$x_{tr.}$	=	distance to transition, m

Y	=	distance normal to flow, m
Z	=	spanwise distance, m
α	=	angle of attack, deg
Δ	=	difference
$(\bar{\delta}^*), \delta^*$	=	(averaged) displacement thickness, m
δ_{99}	=	boundary-layer thickness, m
ϵ	=	angle offset, deg
θ	=	momentum thickness, m
κ	=	von Kármán constant
λ	=	serrations wavelength, m
Π	=	wake parameter
ν	=	kinematic viscosity, m ² /s
φ	=	serrations flap angle, deg

Subscripts

eff.	=	effective
geom.	=	geometrical
lam.	=	laminar
min.	=	minimum
max.	=	maximum
norm.	=	normalized
p.s.	=	pressure side
ref.	=	reference
scaled	=	scaled value
s.s.	=	suction side
turb.	=	turbulent
1/3	=	1/3 octave band
1/12	=	1/12 octave band
∞	=	related to freestream

Superscripts

close	=	closed section
corner	=	corner of the airfoil
open	=	open section
scan plane	=	entire scan plane
+	=	in wall units

I. Introduction

THE acoustic fluctuations originating from the trailing edge (TE) of an airfoil due to interaction of the surface pressure fluctuations induced by the turbulent boundary layer (TBL) [1,2] are responsible for noise emission in a variety of industrial applications,

Received 12 January 2022; revision received 20 May 2022; accepted for publication 25 August 2022; published online 8 December 2022. Copyright © 2022 by the authors. Published by the American Institute of Aeronautics and Astronautics, Inc., with permission. All requests for copying and permission to reprint should be submitted to CCC at www.copyright.com; employ the eISSN 1533-385X to initiate your request. See also AIAA Rights and Permissions www.aiaa.org/randp.

^{*}Ph.D. Candidate, Section Aircraft Noise & Climate Effects, Faculty of Aerospace Engineering; s.luesutthiviboon@tudelft.nl.

[†]Ph.D. Candidate, Section Wind Energy, Faculty of Aerospace Engineering; l.t.limaporeira@tudelft.nl.

[‡]Associate Professor, Section Wind Energy, Faculty of Aerospace Engineering; d.ragni@tudelft.nl.

[§]Assistant Professor, Section Wind Energy, Faculty of Aerospace Engineering; f.avallone@tudelft.nl.

[¶]Professor, Section Aircraft Noise & Climate Effects, Faculty of Aerospace Engineering; m.snellen@tudelft.nl.

for example, in aviation and wind-turbine industries [3,4]. This so-called turbulent boundary layer trailing-edge (TBL–TE) noise represents a main setback in the deployment and growth of those industries. There have been rigorous research efforts to understand, model, and mitigate the TBL–TE noise [2,5,6]. Previous literature has indicated strong needs to validate modeling strategies of the TBL–TE noise and new computational simulation algorithms [7–9] against reference experimental datasets with well-characterized inputs and inaccuracies [7]. One of the most remarkable attempts to create such a reference database for the TE noise problem is the Benchmark Problems for Airframe Noise Computations (BANC) workshop (category I, TE noise). Up to the fifth edition of the workshop (BANC–V), the presented datasets feature aeroacoustic data of a symmetric NACA 0012 airfoil and cambered DU96–W180 and NACA 643–618 airfoils with a straight TE in the chord-based Reynolds number Re_c range from 1×10^6 to 1.5×10^6 [8,9].

The published BANC results left several open questions, as the need to explain the influence of Re_c on the measured TE noise. The narrow Re_c range of the benchmark dataset (1×10^6 to 1.5×10^6) neither is representative of industrial airfoil applications (usually $\geq 3 \times 10^6$) nor covers the range upon which existing semi-empirical TE noise prediction methods are based or where academic studies are carried out [7]. For example, semi-empirical prediction methods such as the one of Brooks et al. [6] or anechoic wind-tunnel measurements [10] are based on data acquired at $Re_c \leq 1 \times 10^6$. This issue has partially been addressed in the work of Ferret Gasch et al. [7], in which the aeroacoustic data of two cambered airfoil models from Siemens Gamesa are tested up to $Re_c = 3.7 \times 10^6$. However, there are still some unexplainable phenomena, for example, a noise increase hump in the far-field noise spectra, which could be attributed to the self-noise of the airfoil, and differences in wind-tunnel setups, in other words, blockage effects and aspect ratios. The authors hypothesized that the noise increase hump resulted from the post-processing method of the far-field acoustic signals. To date, the BANC dataset is available for a scattered Re_c range where the available data and postprocessing protocols differ per campaign. Moreover, boundary-layer parameters at the TE are not consistently available in every dataset, being insufficient for analytical TE noise prediction models. Therefore, Ferret Gasch et al. recommended testing an airfoil with known aerodynamic characteristics with the same postprocessing technique among different institutions.

Currently, datasets available in the BANC category I workshop feature only TBL–TE noise data from airfoils without any TBL–TE noise reduction devices. The lack of well-characterized and documented data of the TBL–TE noise reduction obtained with such devices contrasts with the growing interest and application of them. Among other TBL–TE noise reduction technologies, TE serrations have been widely studied due to their simplicity and robustness [11–15] and are, in fact, an established way of mitigating wind-turbine blade noise, reducing about 3 dB(A) in average [16,17]. Besides, many computational and experimental research works in the past decades have also been focusing on optimizing the TE serrations as well as other alternative devices for the TBL–TE noise reduction [2,18]. Therefore, the current BANC dataset may not completely meet the need for academic and industrial research.

This work addresses the need for a new dedicated aeroacoustic dataset, which will be added to the current BANC framework for TE noise of airfoils. In this new work, a symmetric NACA 633–018 airfoil from the six-series NACA airfoil family is tested with a baseline straight TE and several serrated TE configurations in a broader range of Re_c . For this airfoil, the change of the aerodynamic characteristics in relation to the flow features, for example, Re_c and angle of attack, is known, reported [19], and predictable [20]. The symmetric geometry of the airfoil additionally helps define an accurate zero-lift angle, at the same time allowing one to studying pressure distributions very similar to the ones of profiles usually employed on wind turbines, once placed at a different angle of attack [21].

To achieve the largest Re_c number range possible, two NACA 633–018 models having different chord lengths have been tested in two different wind tunnels. A model with a chord of 900 mm, manufactured by the Technical University of Denmark (DTU), was tested in

the Low-Turbulence Tunnel (LTT) of Delft University of Technology to cover the high Re_c range ($Re_c \geq 1 \times 10^6$). A second with a chord of 200 mm, manufactured at Delft University of Technology, was tested in the smaller (open-jet) A-Tunnel facility, where the anechoic conditions allow for a precise assessment of the acoustic emissions in a lower Re_c range ($Re_c \leq 1 \times 10^6$). In addition to the straight (baseline) TE, two TE serration geometries are considered, namely, the simple sawtooth serrations and the recently introduced iron-shaped serration, which, according to the numerical study of Avallone et al. [22], has shown the ability to achieve a higher maximum TBL–TE noise reduction than the sawtooth serrations. The present experimental work also provides confirmation to this numerical finding.

The aforementioned NACA 633–018 models have also been tested in various other facilities, such as the Stability Tunnel of Virginia Polytechnic Institute and State University [23], the Pour La Cour Tunnel at the Technical University of Denmark (DTU), and the Acoustic Wind Tunnel in Braunschweig in collaboration with the German Aerospace Center (DLR). An extensive endeavor to extend the comparison to different facilities in Europe is on course [24]. This dataset is additionally presented and employed in the Hybrid Anechoic Wind Tunnel (HAWT) yearly activities. The noise reduction data given by various TE serration configurations also fits in the International Energy Association Wind Technology Collaboration Programme Task 39 framework, which focuses on accelerating research and developments of quiet wind turbines.

The paper is organized as follows. Descriptions of the test setup, the test matrix, and the experimental techniques are provided in Secs. II–IV. Subsequently, results and discussions are provided in Secs. V and VI, including the aerodynamic coefficients, boundary-layer parameters, and acoustic results from the two wind-tunnel facilities. The most relevant aeroacoustic data are reported in chord-based Reynolds numbers from 2×10^5 to 3×10^6 and Mach number from 0.04 to 0.2. Finally, the scaling of the acoustic emissions with respect to the boundary-layer parameters at the airfoil TE in both wind tunnels is discussed.

II. Experimental Models and Flow Facilities

A. Airfoil Models and Serration Geometries

To obtain aerodynamic and aeroacoustic results for a wide chord-based Reynolds number range, two models of the same airfoil with different chords c have been tested. For the purpose, a 900-mm-chord and a 200-mm-chord NACA 633–018 airfoil model have been manufactured. Throughout the manuscript, the two models will respectively be referred to as the *low- Re model* (LRM) and *high- Re model* (HRM) for convenience, meaning that the model with the smaller chord was tested at relatively low Re_c ($Re_c \leq 1 \times 10^6$), while the other one was tested at $1 \times 10^6 \leq Re_c \leq 3 \times 10^6$. The NACA 633–018 airfoil profile with the convention for the axis orientation used in the data analysis is presented in Fig. 1. The origin of the reference coordinate system is placed at center of the airfoil TE with X , Y , and Z in the chordwise, vertical, and spanwise directions, respectively.

The NACA 633–018 airfoil profile is symmetric with a maximum thickness-to-chord ratio of 0.18 at $X = -0.661c$. The wing manufactured for the HRM model has a span of $b = 2.22c$, and it was manufactured by Deharde using sheet metal skins covering rib and stringer structures [23]. The LRM has a span $b = 2c$ and was manufactured at Delft University of Technology as an assembly of three solid modular aluminum structures. The TE thickness of both models t_{TE} is $7.5 \times 10^{-4}c$.

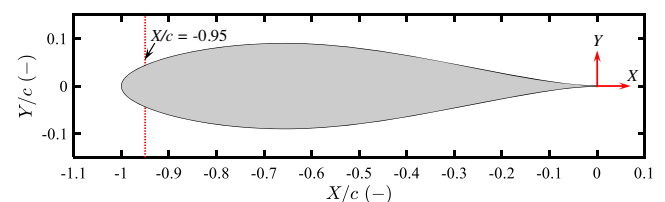


Fig. 1 NACA 633–018 airfoil and axis orientations.

In this study, a careful and detailed characterization of the flow with respect to the boundary-layer transition has been carried out for both natural and forced transition location conditions. The forced transition location helps to ensure comparability of the boundary-layer properties at the TE and therefore the far-field acoustic results from different wind-tunnel facilities, where the inflow turbulence and the natural transition location on a given airfoil may differ [25]. In particular, the tests were carried out for two configurations, in other words, without and with a laminar-to-turbulent forcing transition device, applied to set the transition location at around 5% chord distance from the leading edge, or $X/c = -0.95$ as indicated in Fig. 1. These conditions are referred to as the *clean* and *forced* configurations, respectively. For the latter condition, zig-zag strips were applied at $X = -0.95c$ on both the suction and the pressure sides. Detailed specifications of the turbulators are provided in Fig. 2. On both the LRM and HRM, the boundary-layer state was verified by scanning a stethoscope probe downstream of the turbulator strip along the entire span. The stethoscope comprises a Brüel and Kjær 4134 microphone and a Brüel & Kjær 2619 preamplifier. The stethoscope was also used on the clean configuration to detect the natural transition location. It is worth highlighting that, for both the LRM and HRM in the clean configuration, the boundary layer at the TE is

turbulent. For the LRM, it has been found that the same aeroacoustic behaviors are consistently replicated with distributed carborundum particles with a nominal size of 0.42 mm (Grit No. 46) on a 0.6-mm-width and 0.1-mm-thick base tape, following the guideline of Brashlow et al. [26], installed at the same chordwise location. The combined thickness of the carborundum particles and the tape strip is similar to the one of the zig-zag strip. However, for reproducibility, it is motivated to use only the zig-zag strip for the remainder of this paper because the actual transition location triggered by the carborundum particles may vary along the span, depending on the spanwise particle distribution density [25].

TE serrations were installed on the airfoil and tested under the forced transition location only to ensure reproducibility of this benchmarking noise database when the airfoil is tested in a different wind-tunnel facility or is simulated in a numerical study. Two geometries shown in Fig. 3 are considered: namely, the sawtooth and the iron serrations. These serration geometries are chosen from a numerical study of Avallone et al. [22], which found an additional noise attenuation given by the iron serrations compared to the more conventional sawtooth counterpart, due to minimized scattering at the curved and (almost) tangent roots. The serrations have wavelength $\lambda = 0.05c$, and $2h = 0.1c$, where h is the serration peak amplitude,

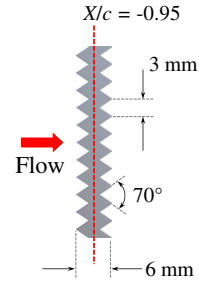
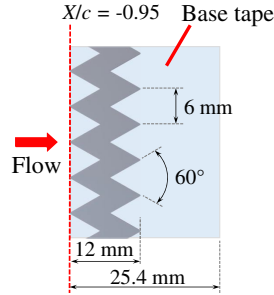
Airfoil model	Turbulator specifications		
	Transition element	Installation tape	Drawing
LRM	Glasfaser-Flugzeug-Service GmbH Zig-zag turbulator Thickness: 0.5 mm Width: 6 mm Angle: 70°	None	
HRM	Glasfaser-Flugzeug-Service GmbH Zig-zag turbulator Thickness: 0.4 mm Width: 12 mm Angle: 60°	Aerovac blue flash tape Thickness: 0.08 mm Width: 25.4 mm	

Fig. 2 Boundary-layer forced-transition device parameters.

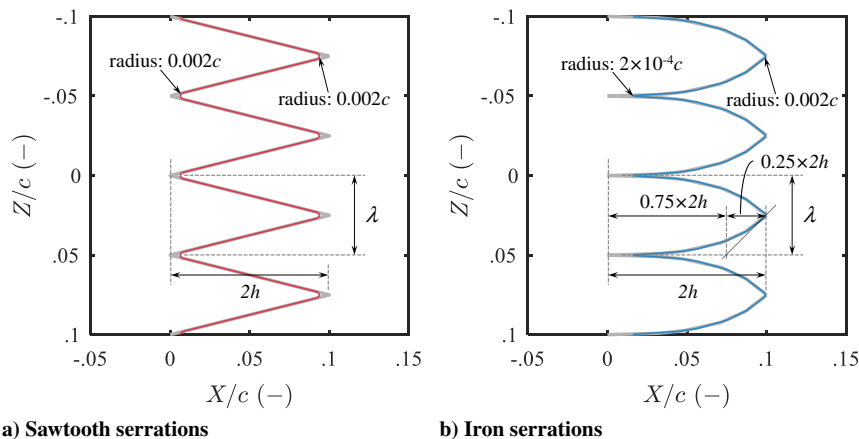


Fig. 3 Drawings of the TE serrations used on the airfoil compared to the geometry used in the simulation of Avallone et al. [22].

following the guidelines given by Gruber et al. [12]. For the experiments, the serrations for both airfoils were produced from a 1-mm-thick stainless steel plate using wire cutting. The serrations feature minimum manufacturing corner radii of $2 \times 10^{-3}c$ and $2 \times 10^{-4}c$ (see Fig. 3). Both serrations were installed with a 0 deg flap angle φ , in other words, parallel to the chord. The sawtooth serration was also tested with flap angles of $\varphi = \pm 8$ deg on the LRM and $\varphi = 4$ deg on the HRM with respect to the chord line, where the positive φ denotes deflection toward the pressure side [27]. Installation of the serrations on the airfoil models differ for the LRM and the HRM. For the LRM, the TE insert starting at $X = -0.2c$ was removed and replaced by the serration clampers which support the serrations on the airfoil. The serration clampers are shown in Fig. 4a. For the HRM, the serrations have an upstream extension of 45 mm, which was used to side mount the inserts to the airfoil using double-sided tapes and aluminum tapes. Note that the actual chord extension is slightly less than $0.1c$ due to the aforementioned minimum radius criteria. Details of the serration installation on the HRM are illustrated in Fig. 4b.

B. A-Tunnel Facility for Low- Re_c Tests: $6 \times 10^4 \leq Re_c \leq 1 \times 10^6$

The A-Tunnel is an open-jet anechoic wind-tunnel facility of Delft University of Technology, where the jet is installed within a room with acoustically absorbent foam wedges. The cutoff frequency of the room is 200 Hz, and the room is characterized as acoustically dead according to the International Organization for Standardization (ISO) 3382 standard [28]. Readers are referred to a paper of Merino-Martínez et al. [29] for further details on the A-Tunnel facility. Different velocity ranges can be achieved by installing outlet nozzles of different contraction ratios. In the present case, two nozzles were employed to achieve Re_c between 0.06×10^6 and 1.0×10^6 , namely, nozzles with a rectangular opening of $Y \times Z = 3.5c \times 2c$ (700×400 mm) for $6 \times 10^4 \leq Re_c \leq 4.6 \times 10^5$ and $Y \times Z = 1.25c \times 2c$ (250×400 mm) for $3.9 \times 10^5 \leq Re_c \leq 1.0 \times 10^6$. For the whole range of flow speeds tested, the turbulence intensity of the freestream is below 0.15% [29].

The LRM was mounted between rectangular side plates, installed and centered downstream from the nozzle outlet (placed at $X = -2.9c$ for both nozzles tested). A photograph of the setup is shown in Fig. 5a. The test section is semi-open to allow for acoustic measurements. The

angle of attack was controlled with a stepper motor with 0.001 deg precision, while the angle bias with respect to the floor was measured by a Wyler Clinotonic PLUS inclinometer with 0.01 deg precision. Because of the semi-open test section, the geometric and effective angles of attack are prone to deviate significantly at high lift conditions [30]. Therefore, when aerodynamic data are of higher relevance than the acoustic data, it is also possible to test the airfoil model in a closed configuration by installing two additional hard-wall panels, as shown in Fig. 5b. Data were collected at geometric angles of attack $\alpha_{geom.}$ ranging from $-21 \text{ deg} \leq \alpha_{geom.} \leq 21 \text{ deg}$ only for the larger nozzle tested. Given the higher airfoil blockage with the smaller nozzle, experiments were only carried out at 0 deg effective angle of attack, in other words, zero lift, for this configuration. Table 1 summarizes all conditions and configurations tested.

C. LTT Facility for High- Re_c Tests: $1 \times 10^6 \leq Re_c \leq 3 \times 10^6$

The Low-Turbulence Tunnel (LTT) facility of Delft University of Technology is a closed-circuit wind tunnel with a contraction ratio of 17.8. In the freestream envelope of the current study between 20 and 70 m/s, the turbulence intensity varies from 0.015 to 0.07% [21,31]. The HRM was mounted on a built-in turntable on an exchangeable octagonal test section, which is integrated into the LTT circuit. The test section has the width, height, and length of $2.00c$, $1.39c$, and $2.88c$, respectively. The airfoil span of $2.22c$ could not fully fit in the section as it was constrained by the test section height. The actual aspect ratio of the airfoil therefore became 1.39, with the remaining portion of the span outside the flow. For this particular test section, the wall panels were treated with Kevlar®-covered melamine wedges to minimize acoustic reflections. An acoustically transparent Kevlar® window [32] was installed on the side panel of the section where a microphone array (see Sec. IV.A) was placed. The aviation-standard Kevlar® 49 T965, with a thickness of 0.12 mm and a weight-to-area ratio of 61 g/m^2 [33], was used in combination with Foam S.T.O.P. open-cell anechoic chamber melamine wedges with a thickness between 7.6 and 15.2 cm, depending on available space. A photograph showing the airfoil installed in the LTT section is provided in Fig. 6. Deviations of the measured surface pressure distribution due to the Kevlar® and melamine walls with respect to the hard-wall configuration [34] are carefully examined and discussed in Sec. IV.B. The background noise

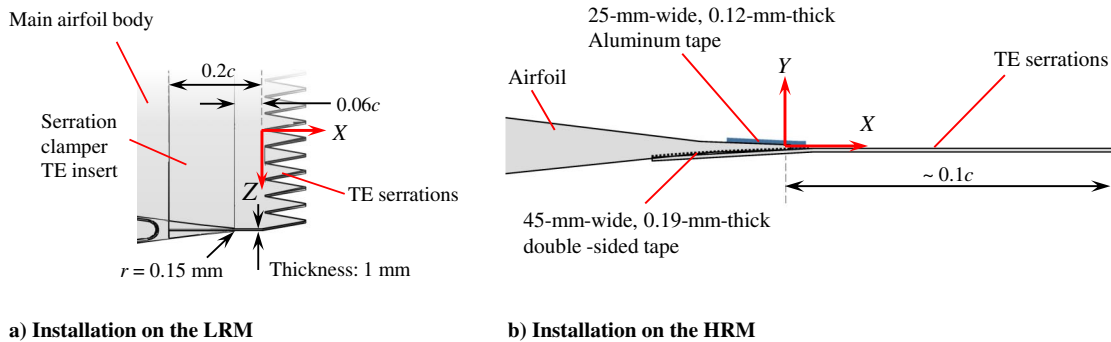


Fig. 4 TE serrations attachment on the airfoils.

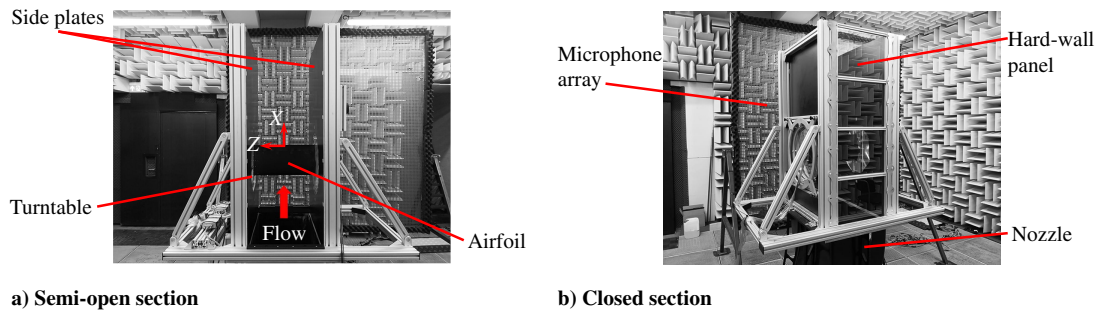
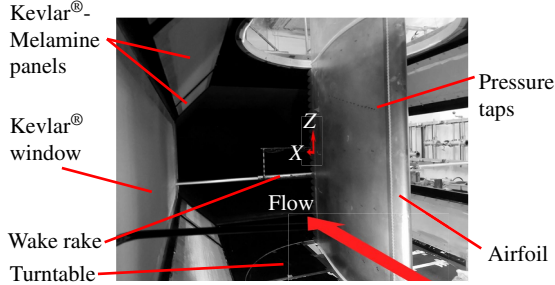


Fig. 5 Installation of the LRM in the A-Tunnel.

Table 1 Data availability matrix

Airfoil model	Wind tunnel facility	Re_c ($\times 10^6$)	u_∞ , m/s	$\alpha_{geom.}$ sweep [start: increment:end], deg	Data availability with respect to $\alpha_{geom.}$, deg				
					Aerodynamics		TBL profiles		
					Static pressure taps	Wake rake drag	Hot wire	PIV	Acoustics
LRM	A-Tunnel, $3.5c \times 2c$ nozzle	0.06	5	[0,6,12,15]	For baseline TE, at all $\alpha_{geom.}$; For serrations, at $\alpha_{geom.}$ for acoustics	N/A	N/A	N/A	0
		0.20	15	$\pm[0:3:9]$, $\pm[9:1.5:24]$, $\pm[24:-1.5:12]$	For baseline TE, available at all $\alpha_{geom.}$ for semi-open and closed sections; for serrations, at $\alpha_{geom.}$ for acoustics	[0:3:18]	0	N/A	$\pm[0, 6, 12, 15, 18]$
		0.26	20	$\pm[0, 6, 12, 15, 18]$	Same as 5 m/s	0	0	N/A	[0, 6, 12, 15]
		0.39	30	$\pm[0:3:9]$, $\pm[9:1.5:24]$, $\pm[24:-1.5:12]$	Same as 15 m/s	[0:3:18]	0	N/A	$\pm[0, 6, 12, 15, 18]$
		0.46	35	$\pm[0, 6, 12, 15, 18]$	Same as 20 m/s	N/A	N/A	N/A	[0, 6, 12, 15]
LRM	A-Tunnel, $1.25c \times 2c$ nozzle	0.39	30	0	0	N/A	0	N/A	0
		0.59	45	0	0	N/A	0	N/A	0
		0.66	50	0	0	N/A	N/A	N/A	0
		0.79	60	0	0	N/A	0	N/A	0
		0.92	70	0	0	N/A	N/A	N/A	0
		1.00	75	0	0	N/A	0	N/A	0
HRM	LTT, Kevlar®-walled section	1.00	16	$\pm[0:2:20]$	For baseline TE, available at all $\alpha_{geom.}$ for Kevlar® and hard walls; for serrations, available up to ± 16 only for Kevlar® wall	Same as p. taps	N/A	[0,4]	$\pm[0:2:8]$, $\pm[8:4:16]$
		2.00	34	$\pm[0:2:20]$		Same as p. taps	N/A	[0,4]	$\pm[0:2:8]$, $\pm[8:4:16]$
		3.00	51	$\pm[0:2:20]$		Same as p. taps	N/A	[0,4]	$\pm[0:2:8]$, $\pm[8:4:16]$, except -2

p. = pressure.

**Fig. 6** Installation of the HRM in the LTT.

properties of the wind-tunnel facility and the transmission loss of the Kevlar® window are discussed in detail in Appendix A.

III. Summary of Available Dataset

By testing the LRM and the HRM in the two wind-tunnel facilities, the experiments can be carried out in a broad and continuous Re_c range. This strategy is visualized in Fig. 7. The chord-based Reynolds number Re_c and geometrical angles of attack $\alpha_{geom.}$ covered in the tests are illustrated. It is also worth highlighting that the tests were carried out at several overlapping Reynolds numbers between different nozzles/facilities. Subsequently, Table 1 summarizes the available data. Measurement techniques mentioned in the table are further explained in detail in the next section.

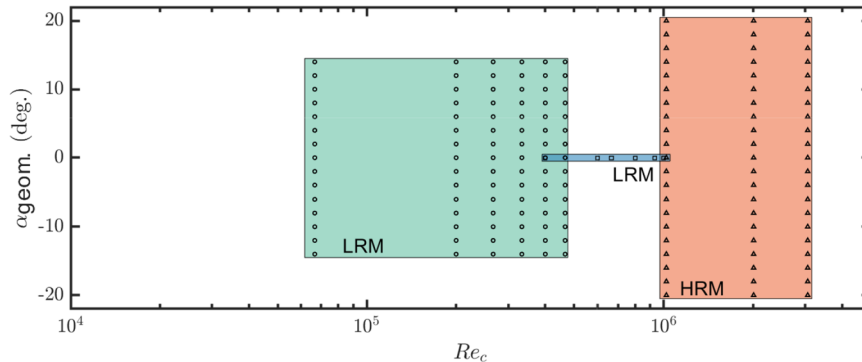


Fig. 7 Illustration of the conditions tested in the test campaigns. The circle and square marks represent the conditions measured during the campaigns with LRM using the $3.5c \times 2c$ nozzle and the $1.25c \times 2c$ nozzle in the A-Tunnel, respectively. The triangular marks represent the experiments carried out with the HRM in the LTT.

IV. Measurement Techniques and Uncertainties

A. Far-Field Acoustic Measurements

For both the LRM and HRM tests, an array of 64 microphones was employed and an acoustic beamforming technique was applied to isolate and quantify the TE noise from the airfoils. The microphones were arranged in a scaled optimized multi-arm spiral configuration [35] facing the X - Z plane. The microphone specifications, array scaling, and positioning relative to the airfoil for the different wind tunnels are specified in Table 2 and illustrated in Fig. 8. Interested readers are referred to Appendix C for the complete microphone array coordinates. The sensitivity factor for the microphones calibration is estimated using a GRAS 42AA piston phone with a reference frequency of 250 Hz and sound pressure level (SPL) of 114 dB.

To isolate noise from the TE region, the source power integration (SPI) [36,37] method within a predefined region of integration (ROI) on the acoustic power maps, obtained from the conventional frequency-domain beamforming [38,39], is used. The steering vector is adjusted to account for the portion of the sound ray paths between the scan plane and the microphones that lies within the flow using the formulation presented by Sijtsma [40]. Specifications of the

postprocessing settings are given in Table 3. The scan plane and the ROI for each campaign are also illustrated in Fig. 8. The background noise level in the wind tunnel is reported in the publication of Merino-Martínez et al. [29] for the A-Tunnel and Appendix A for the LTT.

B. Aerodynamic Coefficient Measurements and Aerodynamic Corrections

1. Lift Coefficient from Surface Pressures

Steady surface pressure distributions were measured on both models via built-in static pressure taps. The lift coefficient c_l is computed from the closed line integral of the pressure coefficients c_p along the airfoil outline s , following Eq. (1),

$$c_l = \frac{\hat{n}_a}{c} \oint_s c_p \hat{n}_s ds \quad (1)$$

where \hat{n}_a and \hat{n}_s represent the unit vectors that are orthogonal to the airfoil angle of attack and to the airfoil surface, respectively.

Table 2 Specifications of the microphone array and the position with respect to the airfoil models

Specifications	Airfoil model	
	LRM ($c = 200$ mm): A-Tunnel	HRM ($c = 900$ mm): LTT
Array width and height in $X \times Z$	$10c \times 5c$	$1.75c \times 0.45c$
Array plane Y location	$-5.00c$	$1.16c$
Microphone model	GRAS 40PH	PUI AUDIO 665-POM-2735P-R
Measurement uncertainty (reconstructed spectra from 50 to 5000 Hz)	± 1 dB	± 2 dB

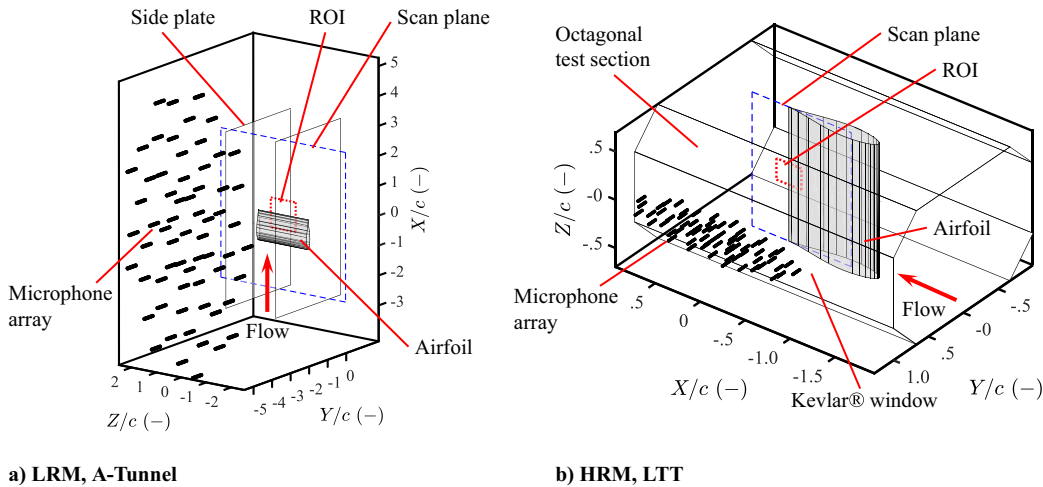


Fig. 8 Microphone array positioning in the two wind tunnels.

Table 3 Specifications the far-field microphone array acoustic signal measurements and processing settings using the SPI beamforming technique

Specifications	Airfoil model	
	LRM ($c = 200$ mm): A-Tunnel	HRM ($c = 900$ mm): LTT
Sampling frequency, kHz	51.2	50.0
Time-domain data snapshot specifications for CSM averaging	5120 samples overlap: 50% Hanning weighing function	2048 samples overlap: 50% Hanning weighing function
Scan plane dimension in $X \times Z$, centered at the origin	$5.00c \times 5.00c$	$1.11c \times 1.39c$
Scan plane resolution	$0.05c$	$0.01c$
Integration region dimension in X and Z , centered at the origin	$1c \times 1c$ span coverage: 200 mm	$0.31c \times 0.25c$ span coverage: 200 mm
Integration lower bound (relative to the maximum value), dB	-6	-6
CSM diagonal removal	No	Yes

CSM = Cross-Spectral Matrix.

The LRM has a total of 28 pressure taps distributed on the airfoil in the middle of the span with a spanwise angle of 15 deg to avoid any possible flow interference resulting from the upstream taps. The pressure taps were connected to Honeywell TruStability HSCDRR025MDAA3 differential pressure transducers of ± 2.5 kPa range and 0.25% full-scale accuracy (± 6 Pa). The HRM has a total of 197 pressure taps. Because of the model installation in the LTT test section, the center of the main pressure tap row was not exactly in the middle of the test section but at about $1c$ from the bottom wall. This main row has 101 pressure taps with a spanwise angle of 10 deg, following the same logic as for the LRM. The main row was the only one used to compute the lift coefficient from this campaign. Three other streamwise-oriented rows spaced $0.28c$ from the main row with 16 taps each were used to confirm the two-dimensional properties of the flow (see Sec. IV.B.4). The pressure taps were connected to a Digital Temperature Compensation (DTC) pressure system featuring six Electronic Pressure Scanner (ESP-HD) scanners with selected ranges for the application (± 2 Pa). Interested readers are referred to Appendix C for the complete pressure tap coordinates for both the LRM and the HRM.

2. Drag Coefficient from Wake Profiles

Drag measurements for both the A-Tunnel and the LTT campaigns were obtained from the momentum deficit in the wake downstream of the model. By assuming the incompressible flow and the Bernoulli theorem, the drag coefficient can be calculated by the method of Jones, which requires the total and static pressure profiles in the wake [41]. For both the LRM and HRM, the pressure distribution was measured by a wake rake. Note that the wake rakes in both wind tunnels were absent during the acoustic measurements. Let c_p denote the pressure coefficients at the wake rake location; the subscripts s and t in $c_{p,s}$ and $c_{p,t}$ indicate that c_p is calculated from the measured static and total pressures, respectively. The drag is then computed by the following integral across the wake [41–43]:

$$c_d = \frac{2}{c} \int_{\text{wake}} \sqrt{c_{p,t} - c_{p,s}} (1 - \sqrt{c_{p,t}}) dY = 2 \frac{\theta_{\text{wake}}}{c} \quad (2)$$

This is equivalent to the momentum thickness across the wake θ_{wake} as shown in the equation.

The wake rake employed in the A-Tunnel has 48 total pressure tubes, spaced 3 mm from each other, and 12 static pressure tubes, spaced 12 mm from each other, placed at $X = 1.0c$. Because of the small model chord, proximity to the trailing edge, and the small angle of attack variation, the wake rake position was fixed, without the need for a traversing system.

The wake rake employed in the LTT has 67 total pressure and 16 static pressure tubes and was placed $X = 0.67c$. A traverse system was used to center the rake with the wake and, during acquisition, to average the drag along the span of the model ($\pm 0.16c$). The center of the wake rake has total pressure tubes spaced by 3 mm, and the whole rake spans 500 mm.

3. Aerodynamic Coefficient Corrections in A-Tunnel

Because of the symmetric geometry of the airfoil, the surface pressure distribution information can be used to determine the effective 0 deg angle of attack in the semi-open configuration. This was done by matching the pressure distribution on both sides of the model. However, in the semi-open configuration at nonzero geometrical angle of attack $\alpha_{\text{geom.}}$, the effective angle of attack $\alpha_{\text{eff.}}^{\text{open}}$ may deviate from the geometrical one due to the distortions of the jet direction by the airfoil circulation. It is assumed that the relationship between $\alpha_{\text{eff.}}^{\text{open}}$ and $\alpha_{\text{geom.}}$ is given by

$$\alpha_{\text{eff.}}^{\text{open}} = -K_B \alpha_{\text{geom.}} \quad (3)$$

where $0 < K_B < 1$ is a correction factor. Brooks et al. [30] provided an analytical formula to determine the value of K_B based on the experimental setup. For this particular setup, the formula gives a value of 0.681 for K_B . This analytical value is confirmed by comparing the pressure on

Table 4 Summary of the angles of attack discussed in the results

LRM, A-Tunnel		HRM, LTT	
$\alpha_{\text{geom.}}$, deg	$\alpha_{\text{eff.}}$, deg	$\alpha_{\text{geom.}}$, deg	$\alpha_{\text{eff.}}$, deg
0	0.00	0.002	0.003
−6	4.02	4.003	4.255
−12	8.04	7.999	8.473

the clean airfoil with baseline TE at $\alpha_{\text{geom.}} = \pm 6$ deg to the pressure distribution calculated with XFOIL [44]. It is found that $K_B = 0.670$, close to the suggested value. For the results presented in this paper, we focus on two nonzero angles of attack. These angles, both geometrical and effective, are summarized in Table 4. It is worth mentioning that the negative sign in Eq. (3) and the sign change in Table 4 (for the LRM) are used to ensure consistency of the sign conventions between the two wind tunnels; in other words, the pressure side of the airfoil always faces the microphone array when $\alpha_{\text{eff.}}$ is positive.

For the results discussed in this paper, the airfoil was tested in the semi-open configuration as shown in Fig. 5a. Nevertheless, information on the angle correction for the closed section configuration (see Fig. 5b) is provided in this section as future aerodynamic test references. The closed configuration posed a small asymmetry in the flow, and therefore a small angle offset ϵ is introduced. The value of ϵ is determined in a manner similar to determining K_B , in other words, by comparing the pressure distribution on the clean airfoil in the close configuration at $\alpha_{\text{geom.}}$ with that of XFOIL. A value of $\epsilon = -0.13$ deg is found, and the relationship between $\alpha_{\text{eff.}}^{\text{open}}$ and $\alpha_{\text{eff.}}^{\text{close}}$ can be written as

$$\alpha_{\text{eff.}}^{\text{open}} = K_B (\alpha_{\text{eff.}}^{\text{close}} + \epsilon) \quad (4)$$

Figure 9 compares the pressure distribution at $\alpha_{\text{geom.}}$ for both semi-open and closed configurations. The predicted pressure distribution from XFOIL using the correction factors introduced in Eqs. (3) and (4) are also given. The closed test section presents an effective value of the angle of attack much closer to the geometrical one, while the semi-open configuration greatly decreases the effective angle of attack. Good agreement between the predicted pressure distribution of XFOIL and the measured ones can be seen for both the semi-open and closed section cases. A slightly larger mismatch is observed on the airfoil suction side in the semi-open section case. It is apparent that flow acceleration around the leading edge that causes the suction peak does not reach a value as high as the theoretical value for a given angle of attack. This could be caused by a combination of multiple factors: first, the flow in the semi-open section has the freedom to diverge, and flow speed reaching the airfoil is not as high as when it

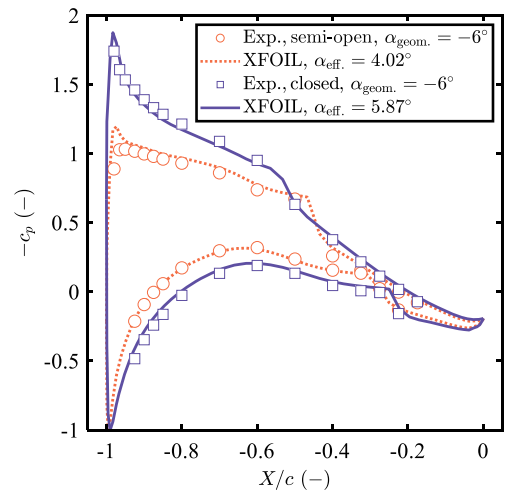


Fig. 9 Measured and predicted pressure distributions on the clean LRM with a baseline TE at $Re = 0.4 \times 10^6$, $\alpha_{\text{geom.}} = -6$ deg in the semi-open and closed section configurations (Exp. = experiments).

leaves the nozzle; second, the fact that the flow is confined by the shear layer, in other words, the finite jet width, exposes the low-pressure region close to the leading-edge that creates the suction peak to static air. This induces the entrance of mass from outside of the jet, in turn weakening the intensity of the suction peak. The latter phenomenon is also visualized in a simulation of Moreau et al. [45].

4. Aerodynamic Coefficient Corrections and Two-Dimensional Flow Investigation in LTT

The LTT correction for the octagonal hard-wall test section can be found in the works of Timmer [31] and Garner et al. [46]. Nevertheless, the modifications applied to the test section wall to improve its acoustic properties may affect the flow conditions and must be assessed. For this purpose, aerodynamic measurements of the baseline airfoil were carried with both Kevlar® and hard-wall configurations. Of major concern, while one side (the wall facing the suction side at positive angles of attack) of the test section was the Kevlar®-melamine panel with a solid back plate for the absorption of the acoustic waves, the opposite side (the wall facing the pressure side at positive angles of attack) was left with a single Kevlar® panel in order to allow the microphone array measurements. This may cause asymmetry between the positive and negative angles of attack tested. Figure 10 shows the comparison of the c_p distributions and c_l curve obtained in both test sections and comparison against XFOIL predictions. From Fig. 10a, in which c_p distributions at $\alpha_{\text{eff.}} \approx \pm 8^\circ$ are compared, a slightly smaller suction peak is captured with the Kevlar® walls. The permeable walls of the Kevlar® section leak air from the ambient room to the test section when the pressure difference is significant, consequently reducing the suction peak. The difference between positive and negative angles of attack is also shown. Using the hard walls as reference, the Kevlar® walls cause a small decrease in the lift (c_l in Fig. 10b) for angles above $\alpha_{\text{eff.}} \approx 10^\circ$ deg at the negative condition caused by the relatively lower

suction peak. An observable difference in c_l can only be found at $\alpha_{\text{eff.}} < -10^\circ$ deg. This is beyond the range of angles considered in the acoustic data analysis (see Table 4).

Additionally, the two-dimensionality of the flow within the test section, both with the Kevlar® and the solid walls, was also verified by comparing pressure distributions from the pressure taps at other spanwise locations to the main one. This comparison is shown in Fig. 11 for $\alpha_{\text{eff.}} \approx \pm 10^\circ$ deg at the highest Re_c . At $\alpha_{\text{eff.}} \approx -10^\circ$ deg, the Kevlar® window causes lower static pressures on the suction side relative to when the solid wall is used. This explains the relatively higher magnitude of c_l at large negative angles of attack seen previously in Fig. 10b. Notably, this trend is seen regardless of the spanwise location Z measured. Therefore, variation of the c_p values along the span are lower than that caused by the difference between the solid and the Kevlar® walls. This confirms the two-dimensionality of the flow in the LTT section within the angle of attack range of interest.

C. Trailing-Edge Boundary-Layer Measurements

Studies have already established the dependencies of the airfoil self-noise spectra on the boundary-layer parameters near the TE [5]. These parameters govern the levels and spectral shape of the measured far-field noise levels. To this purpose, the boundary-layer velocity profiles close to the TE region were measured to provide the TBL parameters necessary for the scaling and comparison of the acoustic spectra. For the A-Tunnel campaign featuring the LRM, the measurements were carried out using the constant-temperature hot-wire anemometry technique. On the other hand, for the LTT campaign featuring the HRM, the particle image velocimetry (PIV) technique was employed. For both campaigns and models, the boundary-layer profiles were extracted very close to the TE at $X/c = -0.02$. More details on the TE boundary-layer measurements are given in the following subsections.

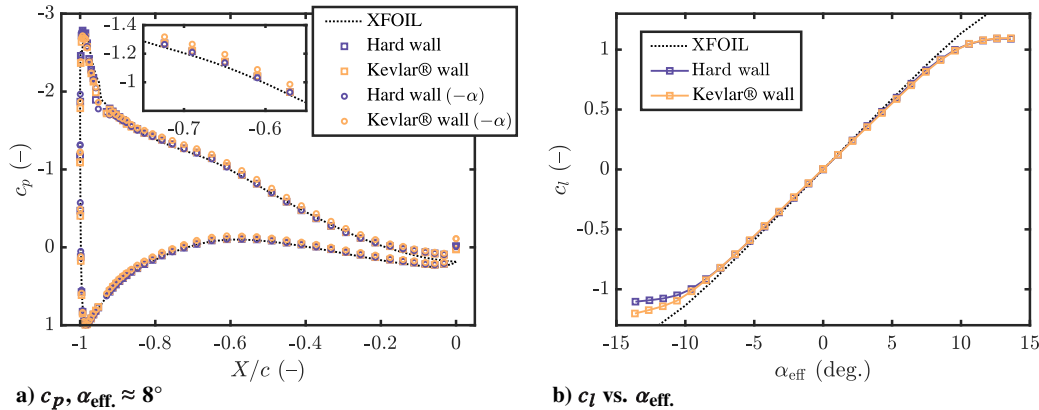


Fig. 10 Comparison of a) c_p distributions and b) c_l curves from the LTT test with hard walls and Kevlar® walls of the baseline NACA 63-018 airfoil at $Re_c = 3 \times 10^6$.

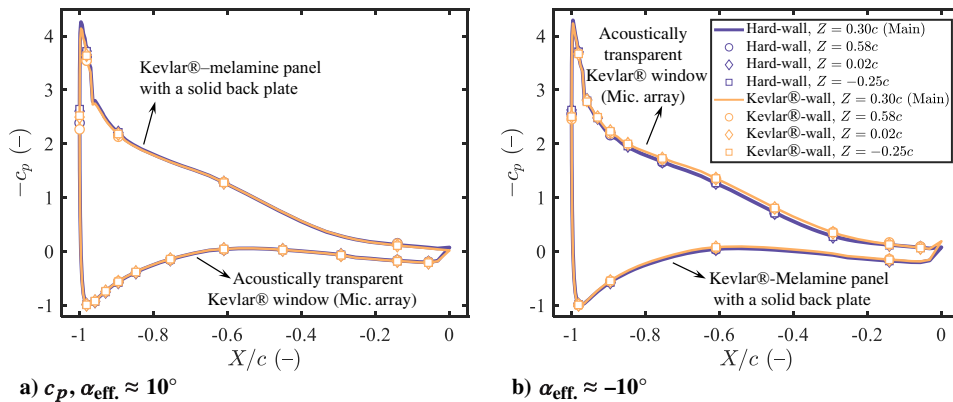


Fig. 11 Comparison of c_p distribution obtained from multiple spanwise pressure tap rows on the baseline NACA 63-018 airfoil in the LTT test section with hard-wall and Kevlar®-wall configurations at $Re_c = 3 \times 10^6$.

1. LRM, Hot-Wire Anemometry

A single-sensor miniature wire probe model 55P15 (boundary-layer type) from Dantec Dynamics was used. The sensitive wire was made of platinum-plated tungsten having a length of 1.25 mm and a diameter of 5 μm . The probe was positioned at $X = -0.02c$ and $Z = -0.3c$ and traversed in the $-Y$ direction using a Zaber LRQ150HL-DE51T3 traverse controller with 0.15 μm accuracy. Conditioning of the sensor was carried out with a TSI® Intelligent Flow Analyzer (IFA-300) Constant-Temperature Anemometry (CTA) module, and acquisition was performed with NI-9234 cards (± 5 V, 24 bits resolution). Data were collected at 71 different points in the $-Y$ direction, with more data points collected near the wall. Each acquisition point took 2 s using the sampling frequency of 51.2 kHz. The calibration used a fourth-order polynomial curve fitting of the output voltages [47] with data from 17 speed–voltage data points logarithmically spaced between the lowest and the highest freestream flow speed u_∞ , which was measured upstream from the airfoil, in other words, close to the nozzle lip. The reference velocity information was taken from a pitot tube installed near the hot-wire probe. The maximum deviation of the actual flow velocity from the flow velocity calculated from the calibrated speed–voltage curve was found to be below 0.2 m/s, or 0.58% of u_∞ .

2. HRM, Particle Image Velocimetry

The flow was seeded with SAFEX fog, and a laser sheet was created at $Z = -0.04c$, in other words, close to the center of the span, using a Quantel EverGreen 200 (200 mJ, dual pulsed, 15 Hz) laser placed in the opposite wall from the microphone array. Two Imager sCMOS (5.5 megapixels, 16 bit, 50 frames/s) cameras were placed at the bottom of the test section, 0.8 m from the illuminated plane. The first camera was positioned along the TE line, to ensure the precision of the in-plane velocities (X - and Y directions), while the second camera was fixed 20 deg in the upstream direction, to allow for stereoscopic PIV postprocessing, obtaining the fluctuations of the velocity in the spanwise (Z) direction [48]. Figure 12 illustrates the setup used for the measurements, and Table 5 summarizes the setup employed and associated uncertainty for the measurement technique. The uncertainty mentioned in the table refers to the instantaneous

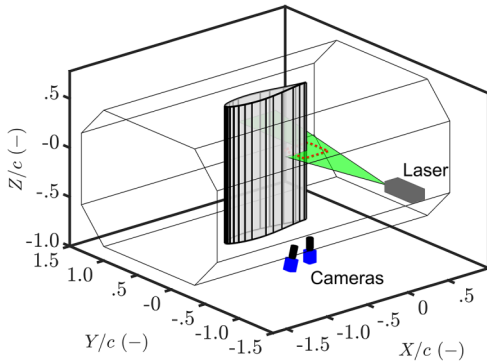


Fig. 12 Schematic of the PIV setup used for the assessment of the boundary-layer properties of the large model.

Table 5 Main parameters of the stereo-PIV measurement technique used to capture the boundary-layer profile during the LTT wind-tunnel campaign

Specifications	Set values
Number of images recorded	1000
Numerical aperture	$f/11$
Digital image resolution, pixels/mm	18
Maximum particle displacement, pixels	15
Field of view ($X \times Y$ mm)	150×100
Vector resolution, mm	0.3
Uncertainty in instantaneous velocity % u_∞	0.7

velocity estimation. The averaging of the 1000 uncorrelated velocity fields reduce the uncertainty to about 0.02% of u_∞ . The velocity field was extracted on a field of $X \times Y = 0.15c \times 0.06c$ centered with the TE. Measurements were carried out only for the forced transition configuration for all the Reynolds numbers for $\alpha_{\text{geom.}} = 0$ deg and additionally ± 4 deg for $Re_c = 2 \times 10^6$.

3. Extraction of Boundary-Layer Parameters

Having obtained the velocity profiles in the direction normal to the wall, the boundary-layer parameters were extracted, for example, the edge velocity u_e , the TBL integral parameters, the displacement thickness δ^* , momentum thickness θ , and boundary-layer thickness δ_{99} . The values of δ_{99} and u_e were obtained from the region where the spanwise vorticity profile becomes constant [49]. The friction velocity u_τ was obtained from the fitting of the logarithmic layer, following the work of Clauser [50]. The fitting procedure results in an uncertainty of 1.5% u_τ in the determination of the friction velocity. The wake parameter Π was calculated based on Eq. (5) from the work of Coles [51]. The implicit equation is solved with a Newton–Raphson method. In the equation, κ , the von Kármán constant, and the parameter C have the values of 0.41 and 5, respectively,

$$2\Pi - \log(1 + \Pi) = \kappa \frac{u_e}{u_\tau} - \log\left(\frac{\delta^* u_e}{\nu}\right) - \kappa C - \log \kappa \quad (5)$$

V. Results: Baseline TE

A. Pressure Distributions

1. Effects of Transition Location and Re_c

Figure 13 shows the pressure distribution over the two models at $\alpha_{\text{eff.}} \approx 0$ deg in the clean and forced configurations. The selected Re_c are 0.4×10^6 and 2×10^6 for the LRM and the HRM, respectively. The results are plotted together with XFOIL predictions at each given condition.

At $\alpha_{\text{eff.}} \approx 0$ deg, the clean configuration in Fig. 13a reveals a laminar separation bubble. For the LRM, the laminar separation bubble starting at $X/c \approx -0.6$ and ending where the flow reattaches at $X/c \approx -0.35$ is clearly visible. This region is shown in the plot inset. However, in this region, the laminar separation bubble is not as visible on the HRM where Re_c is relatively higher. On the other hand, when the tripping strip is applied to force the transition location, similar c_p distributions between the different models and Reynolds numbers can be seen as shown in Fig. 13b. The laminar separation bubble is no longer visible. Additionally, the c_p distribution trends for both the clean and forced configurations are in good agreement with the XFOIL predictions, for both the LRM and the HRM.

Several additional Re_c from both models are included in Fig. 14 to more clearly illustrate the change of the c_p distribution with respect to Re_c . The XFOIL predictions are now omitted. It can be seen from the clean configuration in Fig. 14a that the laminar separation bubble shortens as Re_c increases. This shows that the Re_c effect on the c_p distribution can be seen by joining data from two different wind tunnels. For the forced configuration in Fig. 14b, there is no indication of the laminar separation bubble at any Re_c .

2. Effects of Angle of Attack

The pressure distributions on the LRM and the HRM at $\alpha_{\text{eff.}} \approx 4$ and 8 deg for the clean and forced configurations are shown in Fig. 15. Again, the selected Re_c are 0.4×10^6 and 2×10^6 for the LRM and the HRM, respectively. The results are plotted together with XFOIL predictions at the given conditions.

For the clean configuration, the laminar separation bubble is still visible for $\alpha_{\text{eff.}} \approx 4$ deg, especially for $Re_c = 0.4 \times 10^6$ where it is visible on both the suction and the pressure sides. This is in good agreement with the XFOIL prediction. However, the laminar separation bubble is no longer present for $\alpha_{\text{eff.}} \approx 8$ deg, except for the pressure side of the LRM for $Re_c = 0.4 \times 10^6$.

For the forced configuration, a small deviation of the c_p distribution is observed between the HRM and the LRM on the suction side.

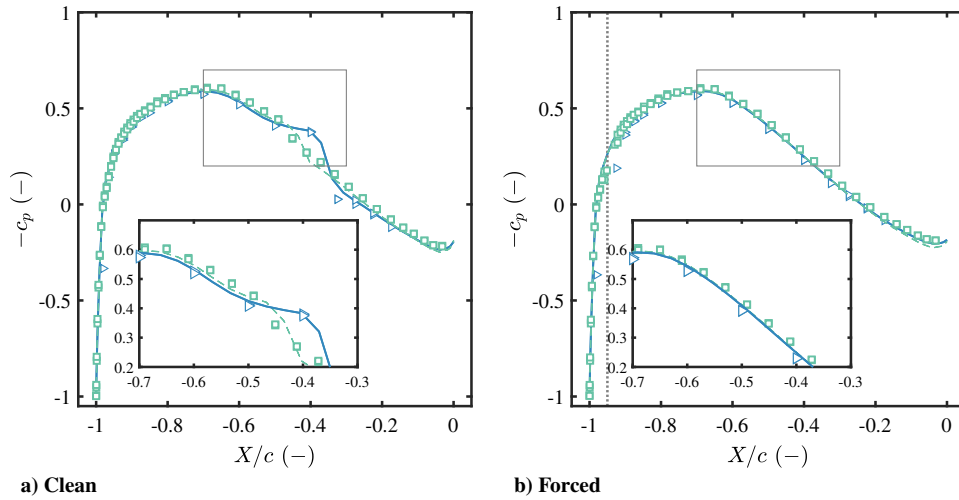


Fig. 13 Comparison of c_p distributions from the A-Tunnel and the LTT tests of the baseline NACA 63₃–018 airfoil with XFOIL predictions at various Re_c and $\alpha_{\text{eff.}} \approx 0$ deg.

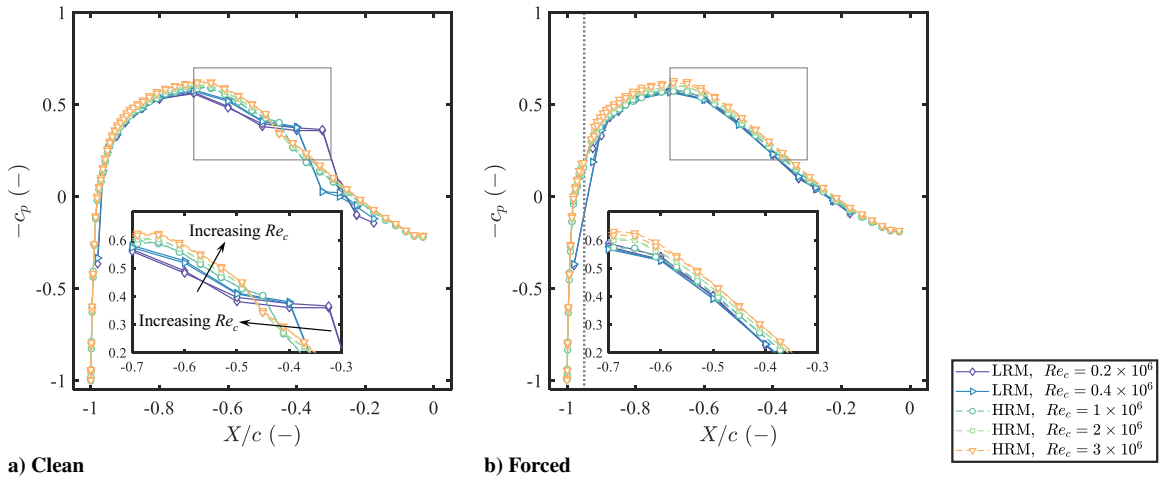


Fig. 14 Comparison of c_p distributions from the A-Tunnel and the LTT tests of the baseline NACA 63₃–018 airfoil at various Re_c and $\alpha_{\text{eff.}} \approx 0$ deg.

The measurements of the HRM feature a slightly lower pressure on the suction side, compared to the LRM. This difference is larger as the angle of attack is increased. Moreover, for the LRM at $\alpha_{\text{eff.}} \approx 8$ deg, the c_p distribution close to the TE on the suction side flattens, indicating flow separation. Therefore, a lower c_l for the LRM is expected for the forced configuration. This is discussed in the next section. Interestingly, for the LRM at $\alpha_{\text{eff.}} \approx 8$ deg, the c_p distribution on the pressure side does not seem to differ from the clean configuration. It is therefore expected that at higher angles of attack the forced transition on the pressure side is not effective.

B. Lift Curves and Drag Polars

The aerodynamic coefficients give an overall picture of the comparisons between the two campaigns. Figure 16 shows the lift and drag coefficients, c_l and c_d , measured on the two models at different $\alpha_{\text{eff.}}$. From the lift curve, the effect of the smaller Re_c at high angles of attack is noticeable. The lift curve for this model exits the linear regime for $\alpha_{\text{eff.}} > 6$ deg. Lower values of c_l beyond the linear regime are observed for the forced transition condition, where the flow separation is seen (see $\alpha_{\text{eff.}} \approx \pm 8$ deg). The stall angle increases with Re_c . In general, the curves agree well with the theoretical $c_l = 2\pi\alpha$.

Similarly, the drag coefficient c_d decreases with the increasing Re_c [52]. The curves follow closely the predictions obtained from XFOIL. For the clean configuration, the critical amplification factors for natural laminar-to-turbulent transition of 9 and 14 were chosen for the LRM and the HRM, respectively, based on the expected turbulence intensity of each wind-tunnel facility [29]. Especially for the

HRM, the measured drag compares well with the predicted one for small angles of attack (-8 deg $\leq \alpha_{\text{eff.}} \leq 8$ deg). For higher angles, the measured drag departs from the ones predicted with XFOIL. At such conditions, the boundary-layer separation is observed sooner than predicted. This is likely because the flow is no longer two dimensional at those angles.

C. Boundary-Layer Parameters at TE Region

Figure 17 illustrates the boundary-layer velocity profiles measured at $X/c = -0.02$. Figures 17a and 17b highlight the difference between the clean and forced configurations for the LRM at 0 deg $\alpha_{\text{eff.}}$. The boundary-layer profiles are shown in dimensional quantities in Fig. 17a, while they are compared to the linear, logarithmic, and wake law predictions in wall units in Fig. 17b. In the latter figure, the black dashed line represents the laminar sublayer ($u^+ = y^+$), the black dotted-dashed lines show the logarithmic law [50], and the colored dotted lines show the sum of the logarithmic layer and the wake layer computed with the wake parameters [51]. In correspondence to Figs. 17a and 17b, Figs. 17c and 17d show the boundary-layer profiles measured for the HRM at $X/c = -0.02$. For this case, the effect of the angle of attack is discussed by comparing 0 deg $\alpha_{\text{eff.}}$ to $\alpha_{\text{eff.}} = 4$ deg. The extensive summary of the extracted boundary-layer parameters for the clean and forced configurations is provided in Tables 6 and 7, respectively.

It is notable from Fig. 17a that the natural transition location condition causes a thicker boundary layer at the TE. This boundary layer presents a relatively lower shape factor $H = \delta^*/\theta$. In Fig. 17b, the forced-to-transition boundary-layer velocity profile departs from

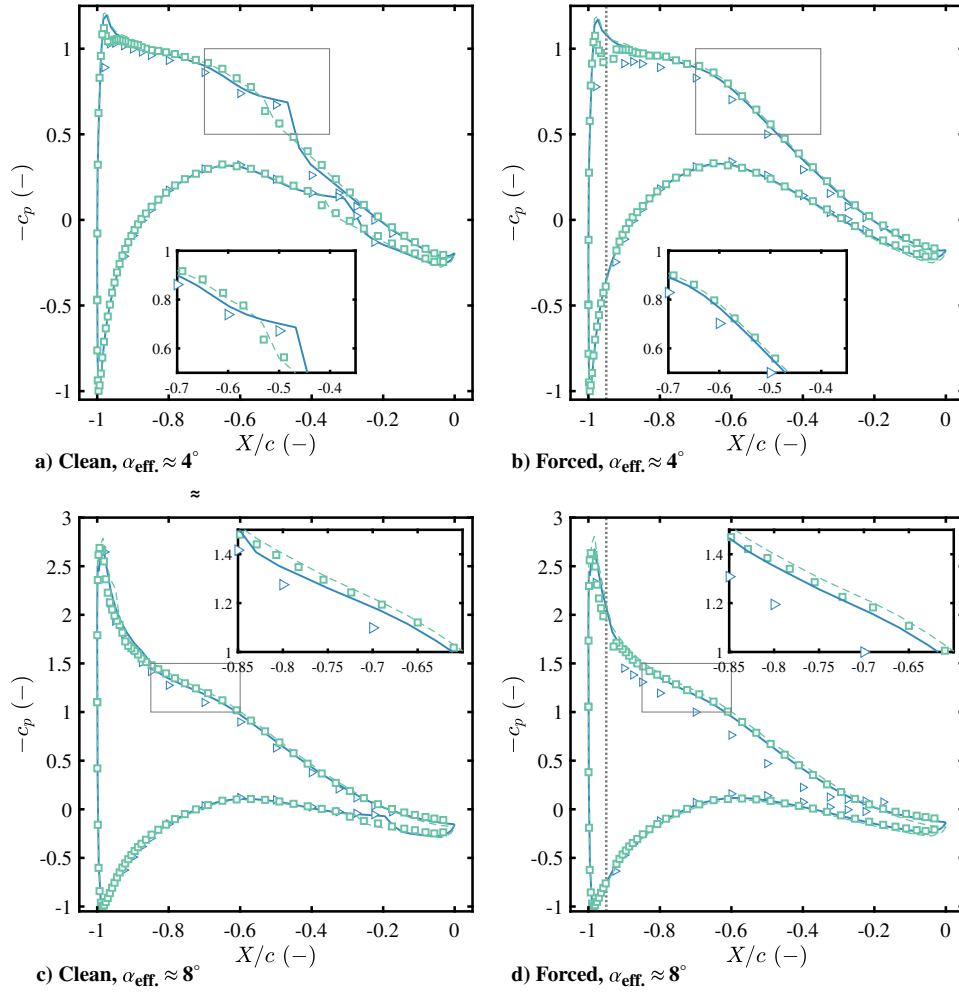


Fig. 15 Comparison of c_p distributions from the A-Tunnel and the LTT tests of the baseline NACA 633-018 airfoil at various Re_c and nonzero α_{eff} .

the logarithmic one [50], resulting in the higher wake parameter Π . This departure is well captured by the curves predicted with the logarithmic and wake laws (the colored dotted lines), following the work of Coles [51].

It can be seen from Fig. 17c that as α_{eff} increases the boundary layer on the pressure side becomes thinner while the one on the suction side becomes thicker. The wake parameter is also strongly influenced by this condition, decreasing on the pressure side and increasing on the suction side (see Fig. 17d and Table 7).

The variation of the boundary-layer thicknesses at $X/c = -0.02$ at $\alpha_{\text{eff}} \approx 0^\circ$ deg with Re_c is shown in Fig. 18a for δ_{99} and in Fig. 18b for δ^* . The graphs contain the data of the LRM (A-Tunnel) experiment with the two different nozzles and of the HRM (LTT) experiment. For Fig. 18a, two trend lines are created for visualization purposes based on the scaling laws shown in Eqs. (6) and (7). These equations come, respectively, from the Blasius solution for the laminar boundary layer and the generic solution of the differential equation of the turbulent boundary-layer growth in [52],

$$\delta_{99,\text{lam.}} = 5 \frac{x_{\text{tr.}}}{\sqrt{Re_{x_{\text{tr.}}}}} \quad (6)$$

$$\delta_{99,\text{turb.}} = K_{\delta_{99}} \left\{ 0.29 \frac{(c - x_{\text{tr.}})^{5/4}}{\left[\left(\frac{c - x_{\text{tr.}}}{c} \right) Re_c \right]^{1/4}} + \delta_{99,\text{lam.}}^{5/4} \right\}^{4/5} \quad (7)$$

where $x_{\text{tr.}}$ and $Re_{x_{\text{tr.}}}$ represent the distance from the leading edge along the chord line where the transition occurs and the Reynolds number based on this distance, respectively. For the clean configuration, the

transition is assumed at $X/c = -0.5$, where the separation bubble is observed for most of the Reynolds numbers (see Fig. 13). The boundary-layer thickness computed from Eq. (7) needs to be scaled with an empirical factor $K_{\delta_{99}} = 2.7$ and 1.5 for the clean and forced transition configurations, respectively. This is necessary as the equations are based on the boundary-layer development on a flat plate; in other words, they do not account for the pressure gradients over the airfoil. The value of the empirical $K_{\delta_{99}} = 2.7$ of the configuration without forced transition is greater due to the effect of the separation bubble on the estimated thickness.

For Fig. 18b, the displacement thickness δ^* variation with Re_c and the tripping condition is compared to XFOIL predictions. The predicted δ^* from XFOIL in Fig. 18b are well in agreement with the measurements. Discrepancies are larger for δ^* for the LRM due to the relatively lower measurement resolution near the wall. The higher shape factor of the boundary-layer profiles for the clean condition case contributes to the fact that the displacement thickness is smaller although the boundary-layer thickness is larger.

The values of δ^* and δ_{99} obtained from XFOIL and the aforementioned equations, in other words, the trendlines in Figs. 18a and 18b, are used for the scaling of the acoustic results.

D. TE Noise Spectra

1. Measured TE Noise Compared to Background Noise and Brooks, Pope, and Marcolini Model

First, the measured far-field noise spectra are compared against the prediction from the semi-empirical model of Brooks, Pope, and Marcolini (BPM) [6] and the background flow noise level measured when the models were absent to assess the reliability. It is worth emphasizing that the BPM model is developed based on an extensive

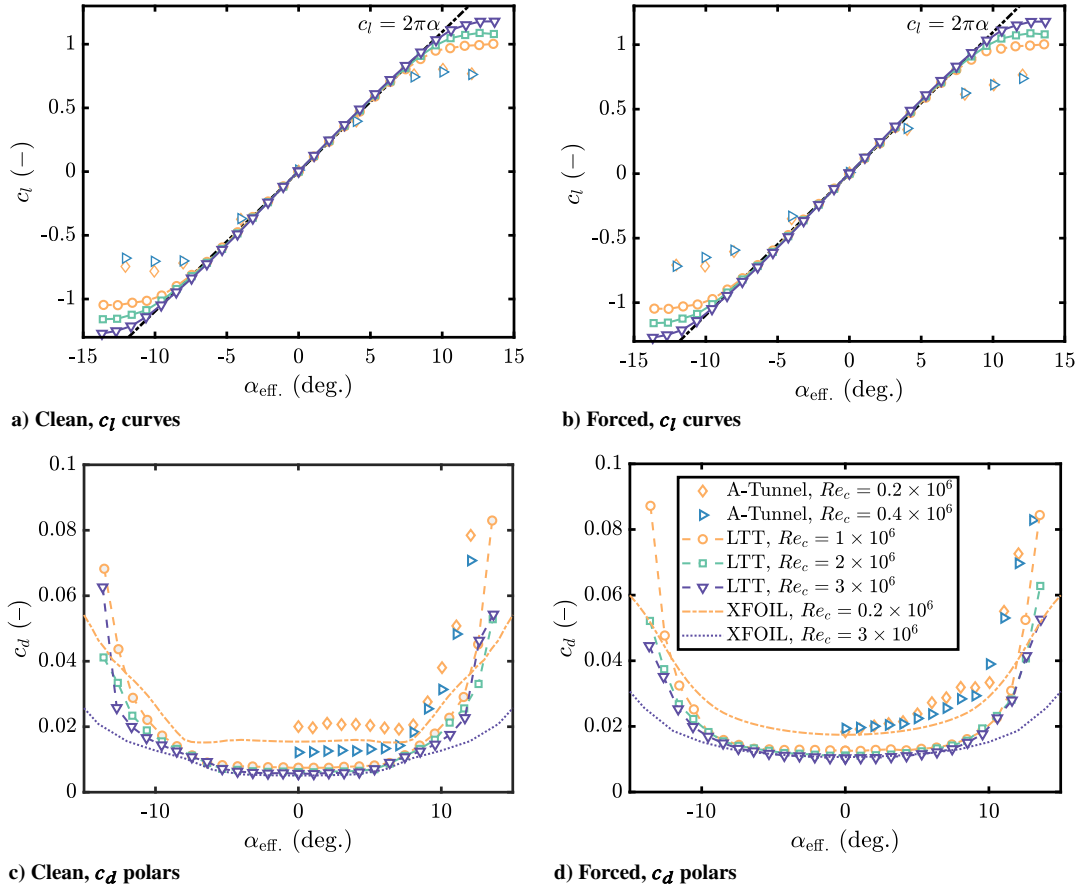


Fig. 16 Comparison of c_l curves and c_d polars from the A-Tunnel and the LTT tests of the baseline NACA 63-018 airfoil at various Re_c .

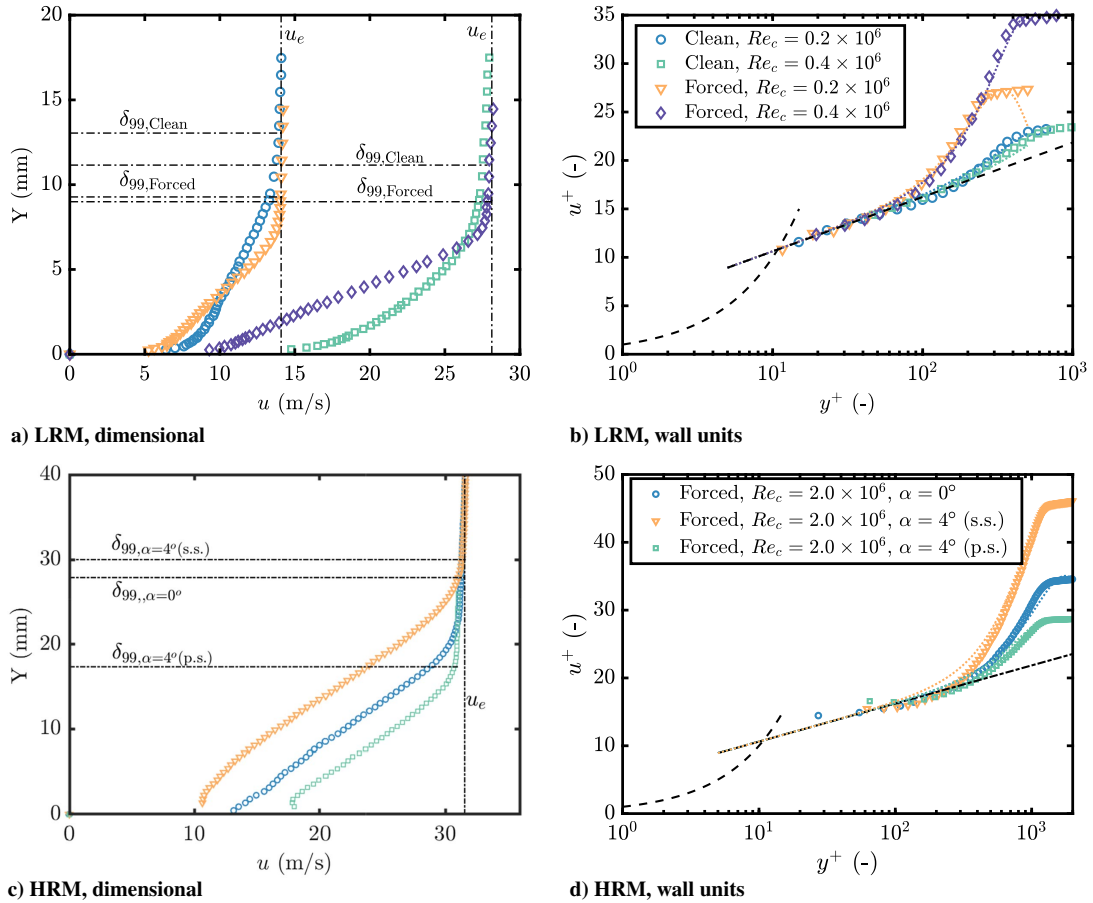


Fig. 17 Comparison of the boundary-layer profiles measured at the TE of both models in dimensional quantities (a and c) and compared against the linear, logarithmic, and wake law predictions in wall units (b and d).

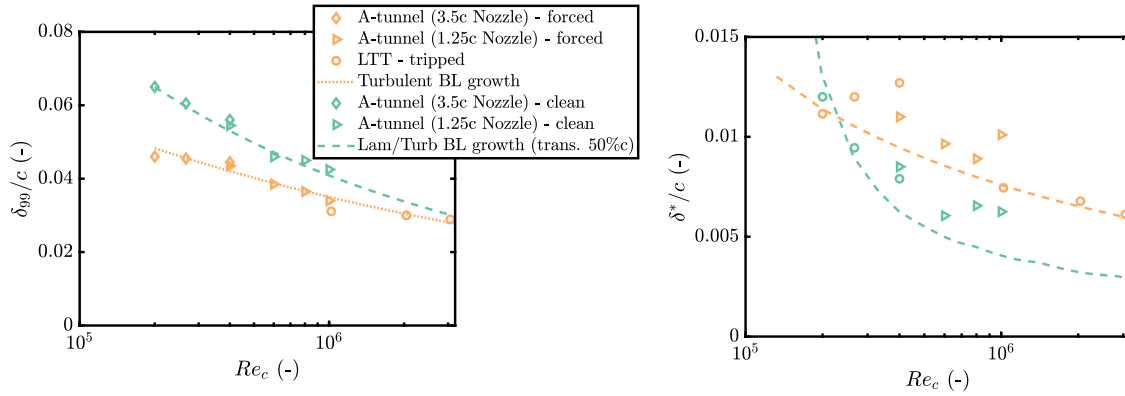


Fig. 18 δ_{99}/c measured at $X/c = -0.02$ and $\alpha_{\text{eff.}} \approx 0$ deg compared against (corrected) scaling laws for turbulent and transitional boundary layers over a plate. The scaling laws are provided in order to guide the reader to the expected trend from the theory and δ^*/c measured at $X/c = -0.02$ and $\alpha_{\text{eff.}} \approx 0$ deg compared against predictions obtained with XFOIL.

experimental dataset featuring a NACA 0012 airfoil, a slightly thinner symmetric airfoil. Therefore, the BPM predictions provide a good reference trend line on the expected far-field SPL spectra variations with Re_c and the clean and forced configurations. However, exact matches are not expected. The extracted boundary-layer properties shown in Tables 6 and 7 are used directly as inputs for the BPM model rather than the scaling laws or XFOIL outputs described previously to avoid additional uncertainties.

Figure 19a shows the comparisons for the LRM measured in the A-Tunnel for the two nozzles (one Re_c per nozzle). The measured far-field SPL spectra, both with and without the LRM, in other words, the empty section, are expressed in the 1/3-octave band format ($SPL_{1/3}$) in order to compare with the BPM model. For the LRM, the $SPL_{1/3}$ spectra of the empty section are obtained by applying exactly the same SPI beamforming technique as described in Sec. IV.A to the measured pressure–time signals.

For the low $Re_c = 0.4 \times 10^6$, the measured $SPL_{1/3}$ levels for the entire frequency range considered are higher than the flow noise in the empty section. The smallest $SPL_{1/3}$ difference of approximately 2 dB is found at the highest frequency: $f = 4$ kHz. The relative spectral slopes and trends between the measured and the predicted $SPL_{1/3}$ spectra are satisfactory for $f \geq 1$ kHz for both the clean and forced configurations. At lower frequencies, the $SPL_{1/3}$ spectral levels tend to exceed the predicted values. Analysis of the source maps in Appendix B shows that this results from the worsened resolution of the source map at relatively low frequencies. Consequently, the sound source at the TE can no longer be discerned from the flow noise from the nozzle. This analysis also shows that the noise from the flow interaction with the side plates is stronger than the TE noise at the relatively higher frequencies. Therefore, these frequencies are not considered in the scaling analysis. For the high $Re_c = 1 \times 10^6$, the measured noise levels are shown to be more severely affected by the background flow noise levels. It is important to

Table 6 Boundary-layer properties measured at the TE of the airfoil at $\alpha_{\text{eff.}} \approx 0$ deg, clean configuration

Model	u_{∞} , m/s	$\alpha_{\text{eff.}}$, deg	Re_c	δ_{99} , mm	δ^* , mm	θ , mm	H	u_e , m/s	u_t , m/s	Π
LRM 3.5c nozzle	15	0	0.2×10^6	13.0	2.40	1.65	1.45	14.1	0.61	0.54
	20		0.3×10^6	12.1	1.89	1.33	1.42	18.6	0.82	0.35
	30		0.4×10^6	11.2	1.58	1.12	1.41	27.8	1.18	0.47
LRM 1.25c nozzle	30	0	0.4×10^6	10.9	1.70	1.07	1.59	29.1	1.25	0.25
	45		0.6×10^6	9.2	1.21	0.75	1.61	41.8	1.87	0.14
	60		0.8×10^6	9.0	1.31	0.84	1.56	56.7	2.37	0.14
	75		1.0×10^6	8.5	1.25	0.77	1.62	69.9	2.77	0.45

Table 7 Boundary-layer properties measured at the TE of the airfoil, forced configuration

Model	u_{∞} , m/s	$\alpha_{\text{eff.}}$, deg	Re_c	δ_{99} , mm	δ^* , mm	θ , mm	H	u_e , m/s	u_t , m/s	Π
LRM 3.5c nozzle	15	0	0.2×10^6	9.2	2.23	1.33	1.68	14.2	0.52	1.7
	20		0.3×10^6	9.1	2.40	1.36	1.76	18.8	0.62	2.3
	30		0.4×10^6	8.9	2.54	1.37	1.85	28.1	0.81	3.0
LRM 1.25c nozzle	30	0	0.4×10^6	8.7	2.20	1.20	1.83	27.7	0.91	2.1
	45		0.6×10^6	7.7	1.93	1.05	1.84	41.4	1.28	2.4
	60		0.8×10^6	7.3	1.78	1.01	1.76	55.1	1.69	2.3
	75		1.0×10^6	6.8	2.02	1.13	1.79	70.9	2.03	2.7
HRM	17	0	1.0×10^6	28	6.6	4.1	1.61	15.3	0.45	2.6
	34	0	2.0×10^6	27	6.1	3.9	1.56	31.5	0.91	2.5
	34	4 (s.s.)	2.0×10^6	30	9.0	4.8	1.87	31.5	0.69	4.8
	34	4 (p.s.)	2.0×10^6	17	3.4	2.8	1.21	31.0	1.08	1.4
	51	0	3.0×10^6	26	5.5	3.5	1.57	47.6	1.34	2.4

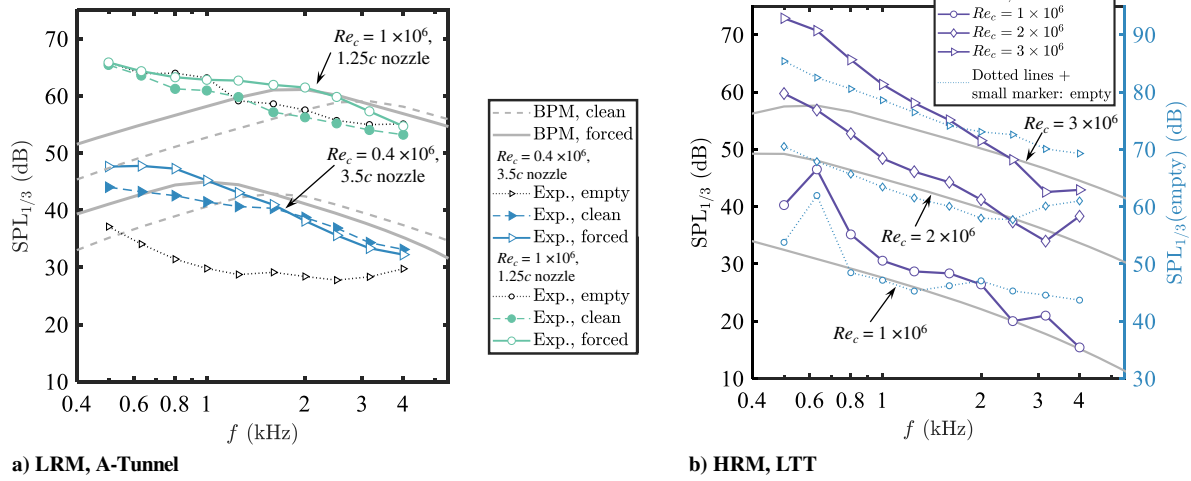


Fig. 19 SPL spectra for the airfoils with baseline TE at various Re_c and $\alpha_{\text{eff.}} \approx 0$ deg considering clean and forced transition configurations compared to the background flow noise levels and the BPM model. The different Re_c and facilities are annotated in the plots (Exp. = experiments).

note that when the LRM was removed the stiffness of the side plates reduced. This caused them to vibrate more freely and thereby cause additional noise, especially at relatively high u_∞ . Therefore, the noise levels from the empty section shown in the plots are likely to be overestimated. Nevertheless, at frequencies above $f = 1.6$ kHz, good agreement between the measured and predicted $SPL_{1/3}$ is found. It can be inferred that the spectra for the forced configuration are more trustworthy because the levels in average are higher than the clean configuration and, therefore, the background flow noise.

A similar comparison for the HRM measurements in the LTT is shown in Fig. 19b. For the HRM cases, only the forced configuration is shown for all Re_c . Because the measurement of the empty section noise level was performed using only one microphone at preselected u_∞ (see Appendix A for the complete narrowband spectra at all u_∞), the empty-section $SPL_{1/3}$ spectra from the closest measured speeds used for each Re_c are shown with a separated vertical axis on the right. For $Re_c = 1 \times 10^6$, a tonal peak is found in the measured $SPL_{1/3}$ at $f = 0.6$ kHz. The comparison indicates that this can be attributed to the background noise. Therefore, to avoid mistaking this tonal noise increase as part of the airfoil self-noise, the lower $Re_c = 1 \times 10^6$ from the LTT–HRM test is omitted in the further analysis. Variations of $SPL_{1/3}$ with Re_c are in line with the prediction for $f > 1$ kHz. It can also be seen that the slopes of the $SPL_{1/3}$ spectra from the airfoil TE region are higher than those of the single-microphone empty-section noise measurement. This could be attributed to the spatial filtering of the beamforming, which improves with increasing f .

2. Effects of Transition Location and Re_c

Figures 20a and 20b show the measured $SPL_{1/3}$ for the clean and forced configurations with the baseline TE measured in the A-Tunnel (LRM) and the LTT (HRM), respectively. Only $\alpha_{\text{eff.}} = 0$ deg is considered, while the nonzero $\alpha_{\text{eff.}}$ will be discussed in upcoming figures.

For the frequency range considered, the effects of the forced transition location on $SPL_{1/3}$ spectra become visible from $Re_c = 0.4 \times 10^6$ onward. At this Re_c , Fig. 18b indicates that the tripping strip applied causes a thicker δ^* at the TE compared to the case without it. This causes a noise increase on the former configuration of up to 5 dB compared to the clean configuration. This trend is in good agreement with the BPM prediction (see Fig. 19a). The frequencies where the noise increase is found are higher for larger Re_c . Additionally, it can be seen that at the overlapping $Re_c = 0.4 \times 10^6$ where the spectra are measured using two different nozzles both the clean and forced configurations $SPL_{1/3}$ collapse well; this confirms that the results from the wide Re_c range can be obtained and interpreted continuously, regardless of the different nozzles.

Similarly, the LTT data are shown in Fig. 20b. For the HRM, the forced transition location does not produce clearly visible difference from the natural one, as the boundary-layer thickness produced for both conditions are similar.

For the LTT measurements of the HRM, the noise created by the vortex shedding from a blunt TE [6] is also observed. Using the suggested Strouhal number based on the TE thickness $St_{\text{TE}} = 0.12$,

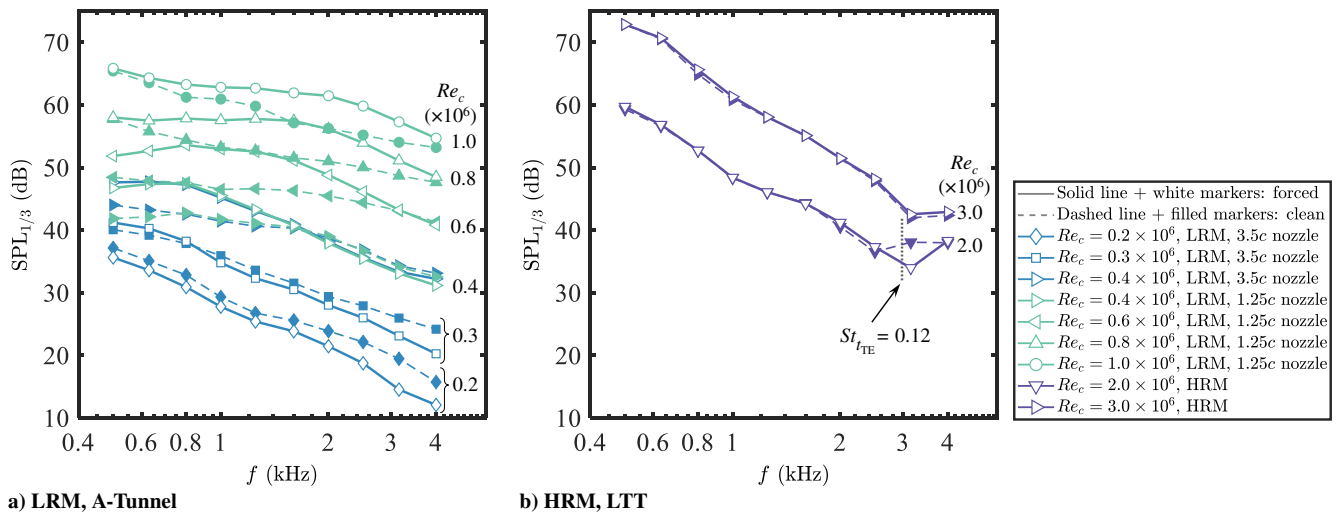


Fig. 20 SPL spectra for the airfoils with baseline TE at various Re_c and $\alpha_{\text{eff.}} \approx 0$ deg considering clean and forced transition configurations.

where $t_{TE} = 1.35$ mm, the frequency at which the peak is expected is marked in Fig. 20b. This frequency is in line with the frequency where the measured $SPL_{1/3}$ from the clean configuration is higher than that of the forced configuration. This is expected because the SPL of the TE bluntness noise varies with $10 \log_{10}(t_{TE}/\bar{\delta}^*)$ [6,53], where $\bar{\delta}^*$ is the averaged displacement thickness at the TE from the suction and the pressure sides. The ratio $t_{TE}/\bar{\delta}^*$ is larger for the clean case as the expected $\bar{\delta}^*$ is smaller than the forced configuration (see Fig. 18b).

3. Effects of Angle of Attack

The effects of the varying effective angle of attack α_{eff} on the $SPL_{1/3}$ spectra are investigated in Figs. 21a and 21b for the A-Tunnel and LTT measurements, respectively. In the same manner as Figs. 20a and 20b, the baseline TE with the clean and forced configurations are considered. Three different α_{eff} mentioned in Table 4 are considered, and the readers are referred back to Figs. 13 and 15 for the c_p distributions at these angles.

For the A-Tunnel data in Fig. 21a, $Re_c = 0.4 \times 10^6$ is considered. For the forced transition configuration, it can be seen that the low-frequency $SPL_{1/3}$ levels ($f < 1$ kHz) increases with α_{eff} . This can be attributed to the thicker $\bar{\delta}^*$ at the suction side. On the other hand, for the clean configuration, a noise increase is observed when α_{eff} increases. The narrowband spectra (omitted for conciseness) indicate that this noise increase is tonal. This is likely due to the acoustic feedback loop of the laminar boundary-layer vortex shedding noise occurring on the pressure side of the airfoil. This effect can also partially be seen for the highest α_{eff} in the forced configuration. This could be because, at high angles, the forced transition was not

effective as discussed in Fig. 15d. Because of the thin TE geometry of the small model ($t_{TE} = 0.3$ mm), the lowest possible frequency for the tonal blunt TE vortex shedding noise is expected to be at $f \approx 6$ kHz. This is beyond the observed frequency range.

For the LTT measurements, shown in Fig. 21b, the Re_c case of 2×10^6 is selected due to the clearest difference between the clean and forced configurations as discussed in Fig. 20b. The values of α_{eff} are selected consistently with Fig. 15. Within the frequency range $1 \text{ kHz} < f < 3.5 \text{ kHz}$, noise reduction of up to 5 dB due to the increasing α_{eff} can be seen. However, the noise increase at lower frequencies is not observed. This could be caused by the LTT wind-tunnel background noise at lower frequencies that hampers the TE noise and all the spectra seem to collapse. This also applies to the higher frequency range at $f > 3.5 \text{ kHz}$. Figures 20b and 21b therefore imply a reliable frequency range for the LTT measurement at this Re_c . Again, the frequency associated with the blunt TE vortex shedding noise is marked by a line. This frequency agrees with the one where the SPLs of the clean configuration exceed those of the forced configuration and can be seen for $\alpha_{eff} \approx 0$ and 4 deg.

E. Scaling of TE Noise

This section is dedicated to scaling of the TE noise measured at the different facilities at different Reynolds and Mach numbers. Figure 22 shows the scaled spectra measured both in the A-Tunnel and the LTT. The measured SPL spectra from both the A-Tunnel and the LTT are examined in the 1/12-octave-band format $SPL_{1/12}$. The forced configuration with the baseline TE at 0 deg angle of attack. The scaled spectra are calculated as [8],

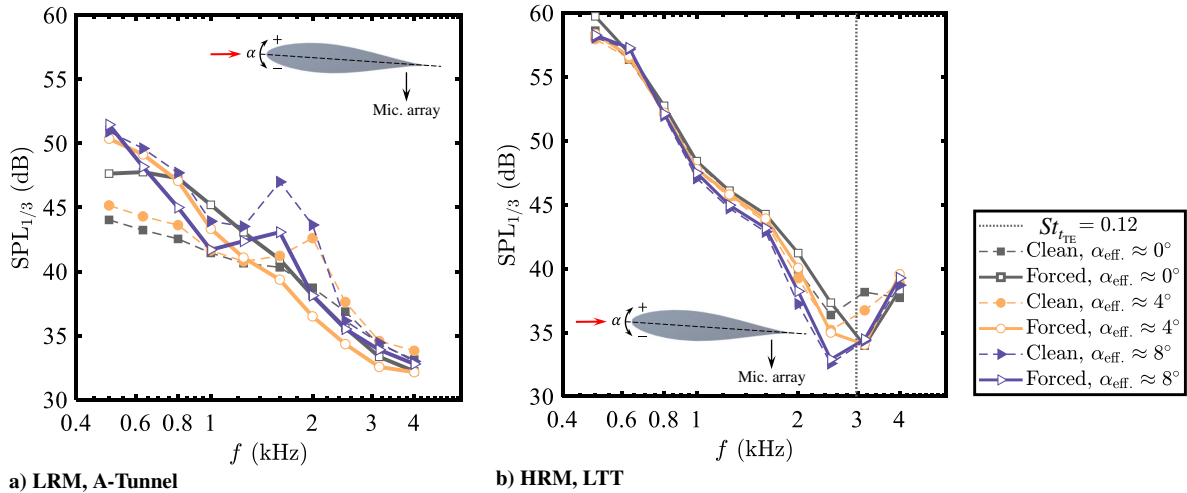


Fig. 21 SPL spectra for the airfoils with baseline TE at various Re_c considering clean and forced transition configurations at various α_{eff} .

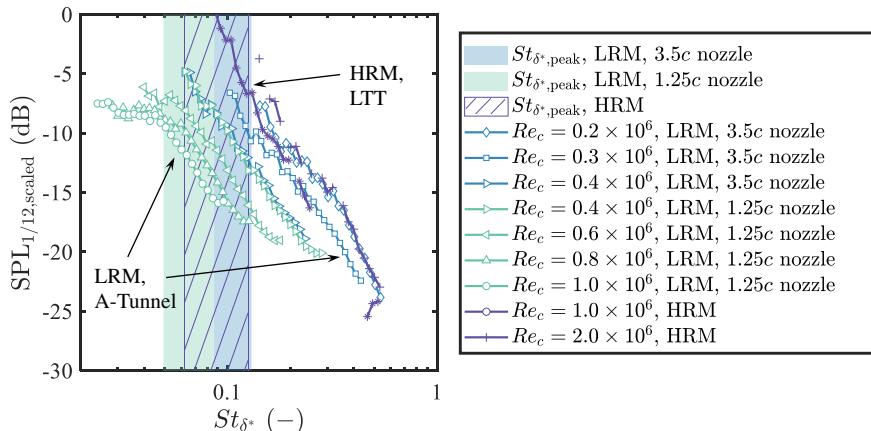


Fig. 22 Scaling of the measured SPL spectra in the baseline TE configuration, based on the Mach number and boundary-layer displacement thickness [see Eq. (8)], for the forced transition condition.

$$\text{SPL}_{1/12, \text{scaled}} = \text{SPL}_{1/12} - 50 \log_{10} M - 10 \log_{10} \delta^* \text{ dB} \quad (8)$$

while the frequency axis is replaced by the displacement-thickness-based Strouhal number: $St_{\delta^*} = f\delta^*/u_{\infty}$. For a scaling as such, Brooks et al. [6] provide an estimation of the peak St_{δ^*} based on the Mach number as $St_{\delta^*} = 0.02M^{-0.6}$. These values are shown based on the Mach numbers in each facility by the shaded areas. Some parts of the spectra are omitted in this scaling due to the low signal-to-noise ratio. This analysis is done based on the examination of the source map presented in Appendix B. As discussed in Fig. 20b, the SPL spectrum of the HRM at $Re_c = 1 \times 10^6$ is largely affected by the LTT background noise at 0.6 kHz. The source map signal-to-noise analysis also showed that fewer than half of the data points at this Re_c case are reliable for the scaling. Therefore, the spectrum for the HRM at $Re_c = 1 \times 10^6$ is excluded in this analysis. However, the spectrum of the LRM at $Re_c = 1 \times 10^6$ is still reliable according to the source map analysis, thanks to the relatively higher signal-to-noise ratio in the A-Tunnel. The latter case is therefore included in this scaling analysis.

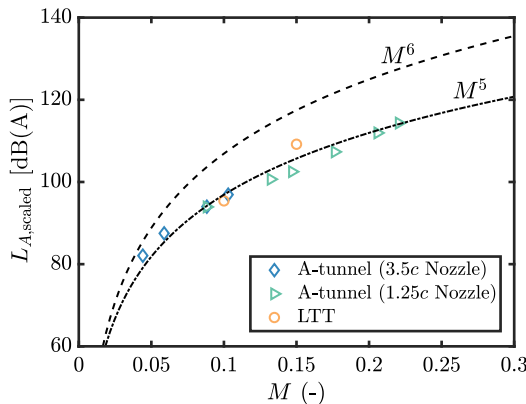
In general, it can be seen that the A-Tunnel data fulfill the low St_{δ^*} range of the spectra that the LTT could not achieve due to the low signal-to-noise ratio of the latter. As Re_c increases, the scaled spectrum shifts toward the lower St_{δ^*} . This trend is often seen when the range of u_{∞} included in the scaling is large, for example, in the work by Brooks et al. [6]. The spectral slopes from both the LRM and HRM are similar. This can be seen by the collapse of the HRM data from the LTT, especially for $Re_c = 2 \times 10^6$ where a wide continuous data range with a high signal-to-noise ratio is available, with the other data points from the LRM.

The result suggests that the experiment featuring the LRM represents mainly the far-field noise emission resulting from the large-scale TBL structures relative to the airfoil chord, whereas the HRM accounts for the smaller scales in the turbulent boundary layer relative to the airfoil chord. Given that the latter represents conditions closer to full-scale applications such as wind turbines, the results indicate that this condition may also be reproduced using only the smaller airfoil model with an improved signal-to-noise ratio in the high-frequency range.

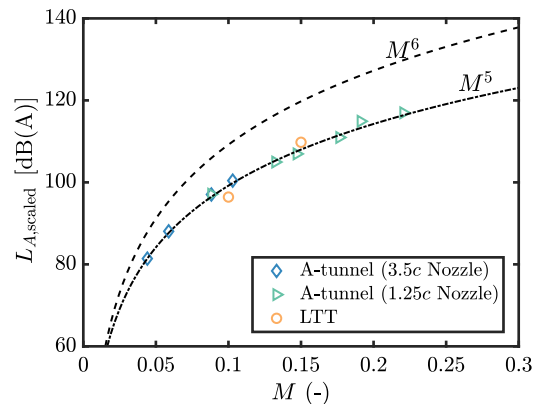
Subsequently, the scaling of the integrated levels with respect to the Mach number is presented in Fig. 23. For this purpose, the A-weighted sound pressure levels L_A are considered. The choice of the A weighting follows the limitations of the measurements at low and high frequencies. The values are scaled according to Eq. (9):

$$L_{A, \text{scaled}} = L_A - 10 \log_{10} \delta^* \text{ dB(A)} \quad (9)$$

Results show the agreement between the measured acoustic data and the hypothesized M^5 scaling [54] for both clean and forced transition configurations.



a) Clean configuration



b) Forced configuration

Fig. 23 Scaling of the A-weighted sound pressure levels L_A of the baseline TE noise with M for $\alpha_{\text{eff.}} \approx 0$ deg.

VI. Results: Serrated TE

A. Lift Curves and Drag Polars

Figures 24a and 24b compare the lift curves (c_l versus $\alpha_{\text{eff.}}$) of the baseline (straight) TE configuration to various TE serration geometries for the LRM and HRM, respectively. The selected Re_c for the LRM and HRM are 0.4×10^6 and 3×10^6 , respectively, and only the forced transition location configuration is considered. The full overview on the baseline lift coefficients can be found in Fig. 16b.

At $\alpha_{\text{eff.}} = 0$ deg, the serrated TE airfoils produce zero lift for most cases due to symmetry, with an exception for the flapped sawtooth serrations where a slightly higher c_l is found. For nonzero $\alpha_{\text{eff.}}$, the airfoil with the serrated TE provides a slightly higher lift curve slope due to the extended effective chord. For $\varphi = 0$ deg, the lift increase provided by the iron serrations is slightly larger than the sawtooth counterpart. This is expected because the iron geometry has a relatively larger wetted area (see Fig. 3). However, the trend is symmetric for both the positive and negative $\alpha_{\text{eff.}}$. On the other hand, for the flapped sawtooth serrations, the airfoil effectively behaves as a cambered airfoil with the relatively higher lift for the positive $\alpha_{\text{eff.}}$, and the trend is no longer symmetric.

Correspondingly, Fig. 24c compares the drag polars (c_d versus $\alpha_{\text{eff.}}$) of the baseline (straight) TE configuration to various TE serration geometries for both the LRM and the HRM. Again, the full overview on the baseline drag coefficients can be found in Fig. 16d. The results from both the LRM and the HRM consistently show a slight increase in drag when the TE serrations are installed. However, the difference in the c_d increments among the different TE serration geometries cannot be discerned by the present experimental approach. This could be limited by the resolution of the wake rake; in other words, the thickness of the serrations (1 mm) is lower than the spacing between the adjacent total pressure probes on the wake rake (3 mm).

B. Boundary-Layer Parameters at TE Region

The boundary-layer parameters measured with the hot wire on top of the LRM with different serration devices are shown in Table 8. The parameters are computed following the same procedure described in Sec. IV.C.

When $\varphi = 0$ deg, the boundary-layer thickness at $X = -0.02c$ is comparable to the baseline TE case. Notably, the serrations are responsible for a local decrease of the boundary-layer momentum and displacement thicknesses. This might be caused by the favourable pressure gradient induced by flow deceleration due to the presence of the serrations. Under a more favorable pressure gradient, the boundary-layer growth rate is smaller.

A stronger influence is observed when serrations are put at an angle with respect to the airfoil symmetry line, in other words, flapped serrations, $\varphi \neq 0$ deg. From the suction side, the boundary layer develops thicker and with a stronger wake layer (higher value of Π), while from the pressure side, the boundary layer is thinner, and the

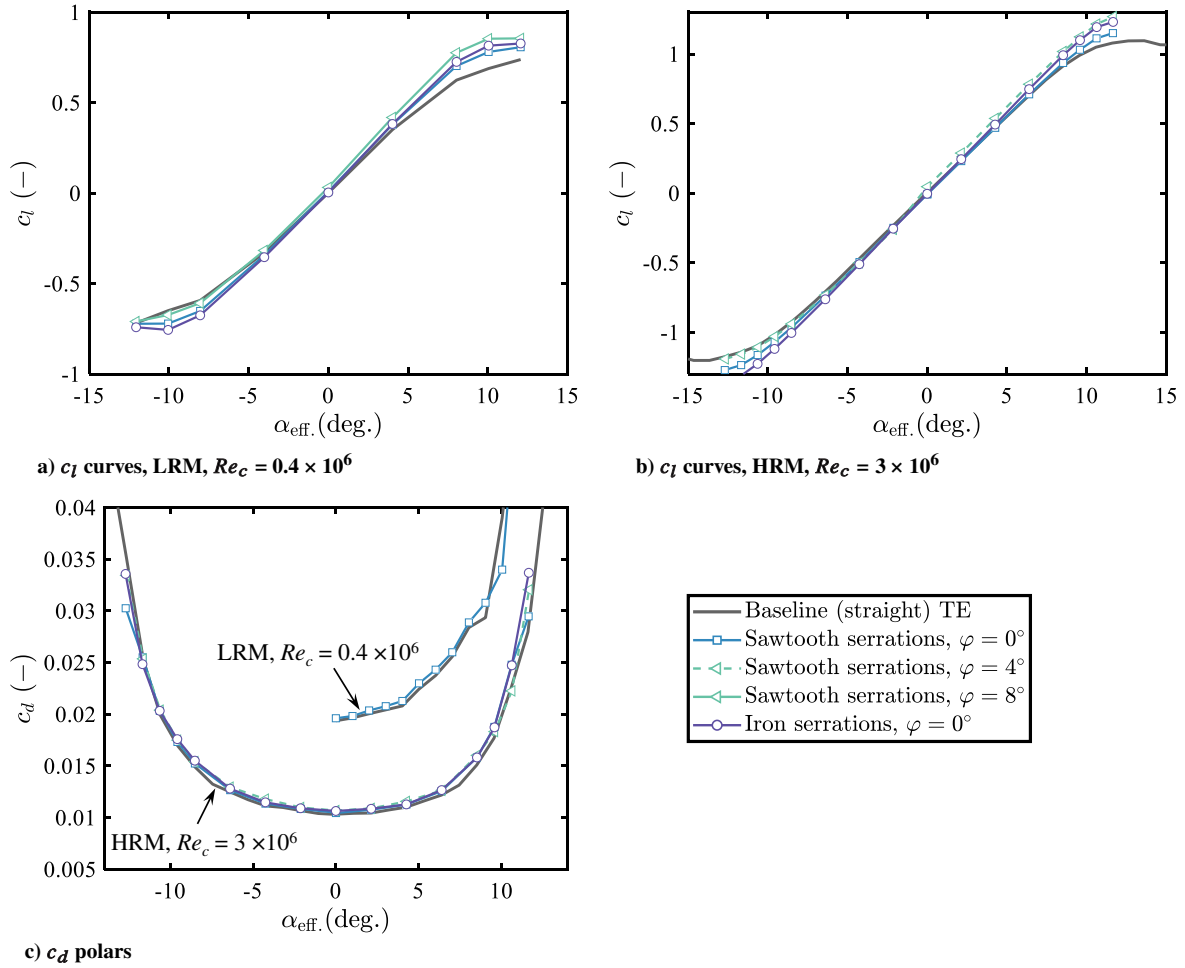


Fig. 24 Measured aerodynamic coefficients with different serration inserts installed. Only the forced transition location configuration is considered.

Table 8 Boundary-layer properties measured at the TE of the LRM with different serration devices at various Re_c and $\alpha_{eff.} \approx 0$ deg

Serration geometry	u_∞ , m/s	Re_c	δ_{99} , mm	δ^* , mm	θ , mm	H	u_e , m/s	u_r , m/s	Π
Baseline	30	0.4×10^6	8.9	2.54	1.37	1.85	28.1	0.81	3.0
Sawtooth $\varphi = 0$ deg	—	—	8.3	2.49	1.33	1.87	28.1	0.82	2.9
Iron $\varphi = 0$ deg	—	—	9.1	2.53	1.34	1.89	28.6	0.81	3.0
Sawtooth $\varphi = 8$ deg (s.s.)	—	—	9.9	2.74	1.41	1.94	27.8	0.75	3.4
Sawtooth $\varphi = 8$ deg (p.s.)	—	—	7.8	2.17	1.21	1.79	28.6	0.91	2.3
Baseline	75	1.0×10^6	6.8	2.02	1.13	1.79	70.9	2.03	2.7
Sawtooth $\varphi = 0$ deg	—	—	6.7	1.81	1.00	1.81	68.5	1.99	2.6
Iron $\varphi = 0$ deg	—	—	6.5	1.83	1.00	1.83	68.5	1.97	2.7
Sawtooth $\varphi = 8$ deg (s.s.)	—	—	6.7	1.97	1.06	1.86	67.9	1.81	3.3
Sawtooth $\varphi = 8$ deg (p.s.)	—	—	6.4	1.78	0.98	1.82	69.9	2.05	2.5

boundary-layer profile follows closely the logarithmic law (smaller value of Π).

Nevertheless, the boundary-layer displacement thickness, used in the remainder of this work for nondimensional representations, does not change with more than 15%. This indicates that the presence of the serrations does not drastically affect the properties of the incoming turbulent boundary layer.

C. TE Noise Spectra Relative to Straight TE

1. Effects of Serration Geometries and Re_c

Figures 25 and 26 show the noise reduction with respect to the baseline TE in 1/3-octave bands $\Delta SPL_{1/3}$ obtained with the different TE serrations in the A-Tunnel and in the LTT, respectively. In the

figures, $\Delta SPL_{1/3} = SPL_{1/3} - SPL_{1/3,ref.}$ dB, where $SPL_{1/3}$ is the noise level of TE serrations cases of interest at selected Re_c and $\alpha_{eff.}$ and $SPL_{1/3,ref.}$ is the baseline TE noise level at the corresponding Re_c and $\alpha_{eff.}$ (see the absolute levels in Figs. 20 and 21). The negative $\Delta SPL_{1/3}$ indicates noise reduction. The effects of increasing Re_c on the $\Delta SPL_{1/3}$ are investigated in the figures where each subfigure accounts for a different TE serrations geometry. Only $\alpha_{eff.} = 0$ deg is considered.

For the given frequency range, the frequency, where the maximum noise reduction is found, appears to increase with the increasing Re_c . This frequency shift follows the work of Gruber et al. [12], who suggest that the $\Delta SPL_{1/3}$ scales with the Strouhal number based on the TBL thickness, thus decreasing with the increasing Re_c . As also

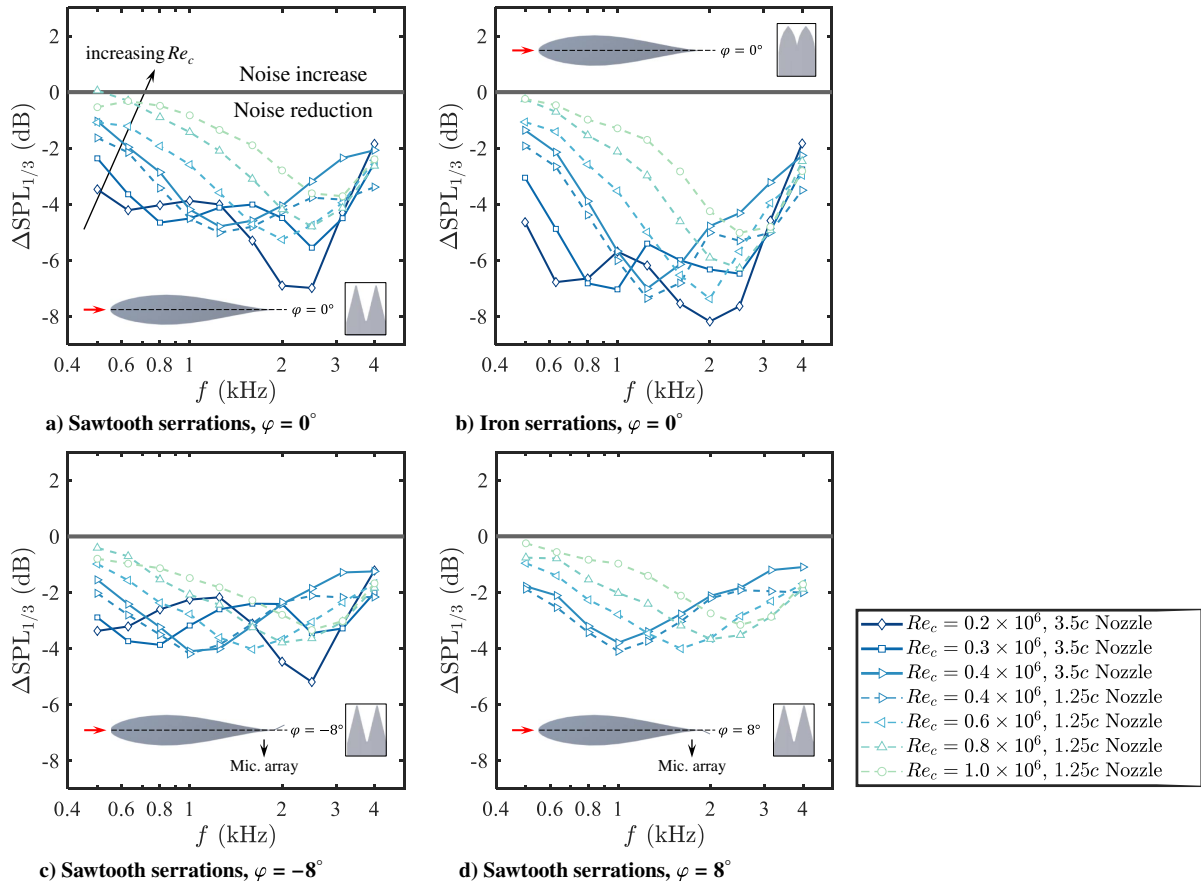


Fig. 25 One-third octave band SPL noise reduction spectra for the LRM under forced transition condition with serrated TEs at various Re_c and $\alpha_{eff} \approx 0$ deg.

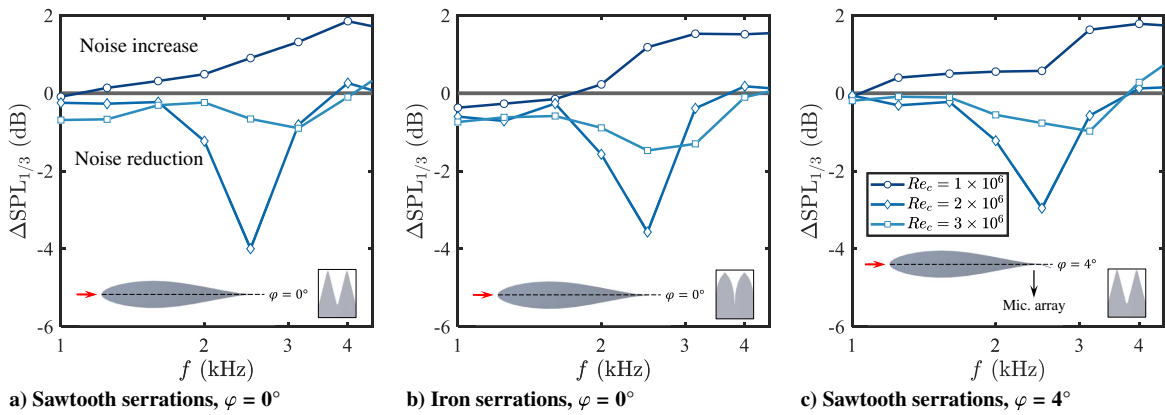


Fig. 26 One-third octave band SPL noise reduction spectra for the HRM under forced transition condition with serrated TEs at various Re_c and $\alpha_{eff} \approx 0$ deg.

presented in other works [12,55], the noise reduction has a maximum that depends on the flow velocity. This maximum is around 5 dB for the sawtooth and 7 dB for the iron-shaped serrations. The results also confirm the higher noise reduction observed for iron-shaped serrations in numerical studies by Avallone et al. [22].

Figure 25 shows that $\Delta SPL_{1/3}$ measured with the large 3.5c and the small 1.25c nozzles is similar up to $f = 2$ kHz. Beyond this frequency, approximately 1 dB additional noise reduction is found when measuring with the small (1.25c) nozzle. This is likely caused by the lower background noise of the fan operating at a smaller mass flow rate with the smaller nozzle (see the A-Tunnel characterization by Merino-Martínez et al. [29]). For the lowest Re_c tested, the measurements show a second peak of noise reduction around $f = 2$ kHz. This feature is observed for both the sawtooth and the iron serration and is also found in the study of Zhou et al. [15], in which

the sawtooth and the iron-shaped TE serrations were tested on a flat-plate at Re_c similar to that of the LRM. This additional noise reduction at relatively higher frequencies could be due to the destructive interference of the high-frequency content in the surface pressure fluctuation occurring close to the serration tip [14,15]. For the flapped sawtooth serration, a lower noise reduction is found compared to the zero-flap one. This is because the airfoil is effectively cambered when the flapped serrations are installed, and the nonzero airfoil loading (see the change in c_l in Fig. 24a) induces formation of a pair of vortices along the edge of the serrations. The lift-induced vortex formation hinders the noise reduction [27].

It is worth highlighting that the background noise levels in the LTT vary largely with the flow speed. In Fig. 19b, it can be observed that at $Re_c = 2 \times 10^6$ the spectra are least affected by the LTT background noise. This implies that, for $Re_c = 2 \times 10^6$, the noise reduction can

most clearly and completely be seen. For the available data, the maximum noise reduction of approximately 4 dB is observed at $f = 2.5$ kHz. The influence of the serration shape on the maximum noise reduction cannot be seen as clearly as for the LRM data from the A-Tunnel. Nevertheless, it can be observed that a slightly lower noise reduction is obtained for the flapped sawtooth serrations compared to the zero-flap counterpart. This is consistent with the finding for the LRM.

2. Effects of Angles of Attack

The influence of increasing α_{eff} on the $\Delta\text{SPL}_{1/3}$ provided by the TE serrations are shown in Fig. 27 for the LRM. The α_{eff} selection is consistent with Fig. 21a as well as the selected $Re_c = 0.4 \times 10^6$. As the angle of attack increases, the noise reduction promoted by the serrated TE decreases. This phenomenon is attributed to the aforementioned formation of the vortex pairs, which is present for both the flapped and the nonflap serrations for nonzero α_{eff} , due to the nonzero c_l (see the change in c_l in Figs. 24a and 24b). Therefore, this effect is more pronounced for the sawtooth serration with positive flap angle ($\varphi = 8$ deg) because the aerodynamic loading over the serration is the highest. This configuration shows noise increase at $\alpha_{\text{eff}} = 4.02$ deg. On the other hand, the noise reduction spectra provided by the sawtooth serrations with the negative flap angle ($\varphi = -8$ deg) is least affected when the angle of attack increases due to the least altered airfoil loading, in other words, smallest change in c_l . This can be confirmed from the lift curves in Figs. 24a and 24b for the positive φ at negative α_{eff} . The same trends are also captured by the experiment with the HRM (see Fig. 28).

D. Scaling of TE Noise Reduction

Figure 29 shows the noise attenuation spectra by the sawtooth serrations with $\varphi = 0$ deg from both the A-Tunnel and the LTT at

$\alpha_{\text{eff}} = 0$ deg and all the Re_c considered in the 1/12-octave band format $\Delta\text{SPL}_{1/12}$. The lift-induced vortex formation hinders the noise reduction [27]. The frequency axes are replaced by the Strouhal numbers based on different length scales. The dashed line shows the predicted noise reduction for the small model configuration given by the analytical model of Lyu and Ayton [13].

For the scaling shown in Figs. 29a and 29b, the Strouhal numbers are based on δ^* and δ_{99} , following the work of Howe [11] and Lyu and Ayton [13], who suggested that the spectrum of noise reduction caused by a serrated TE is dependent only on the serration size with respect to the thickness of the boundary layer. On the other hand, for Fig. 29c, the Strouhal numbers are based on the chord c , following the serration geometry tested in this experiment, which is designed with the same proportion of the airfoil chord. From the spectrum obtained in the A-Tunnel, it is clear that the scaling based on the boundary-layer thicknesses (Figs. 29a and 29b) results in a better match of the *low-St* region in the noise reduction spectrum promoted by the serrations. Nevertheless, the high-frequency cutoff seems to have a different dependency and starts at a lower St for higher Re_c and higher ones for the low Re_c experiments. This observation does not follow the results from Gruber et al. [12], who suggested that the noise increase from the serrations starts at $St_\delta \approx 1.0$. This different dependency of the cutoff band suggests that this region of the spectrum does not follow the large scales of the boundary layer (outer scales) but rather the small ones (viscous or inner scales [56]).

A meaningful collapse between the HRM and the LRM data at relatively lower Strouhal numbers cannot be seen. This is due to the high background noise levels at low frequencies in the LTT test of the HRM, and the relatively large serration with respect to the boundary-layer scales hinders the obtained noise reduction. Therefore, the measured noise reductions within this range are invisible.

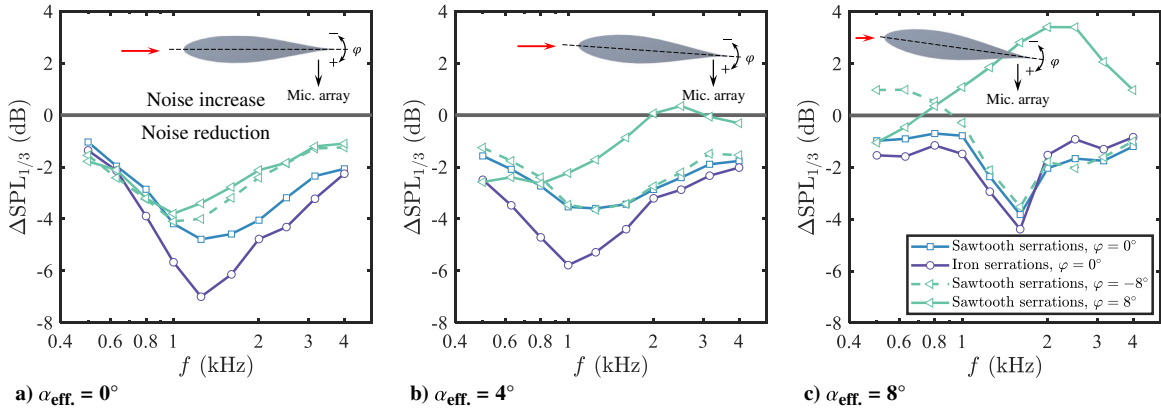


Fig. 27 One-third octave band SPL noise reduction spectra for the LRM under forced transition condition with serrated TEs at $Re_c = 0.4 \times 10^6$ and various α_{eff} .

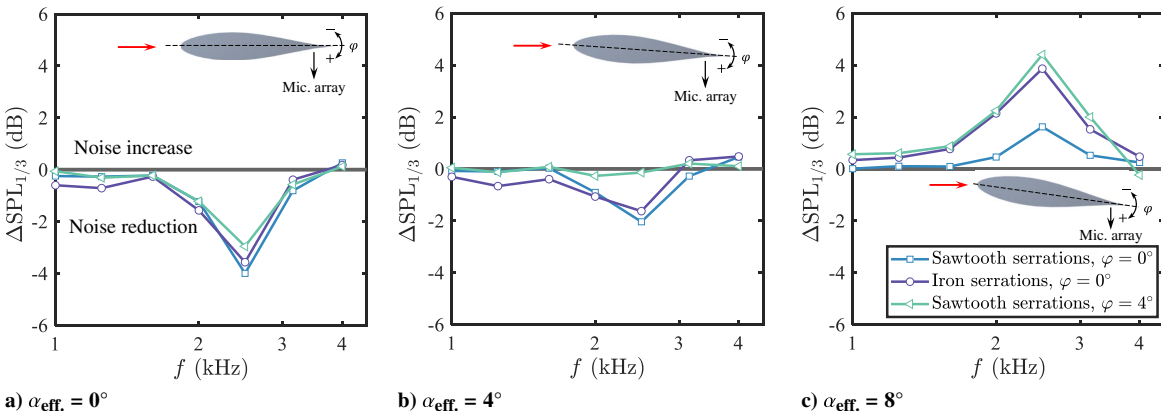


Fig. 28 One-third octave band SPL noise reduction spectra for the HRM under forced transition condition with serrated TEs at $Re_c = 2 \times 10^6$ and various α_{eff} .

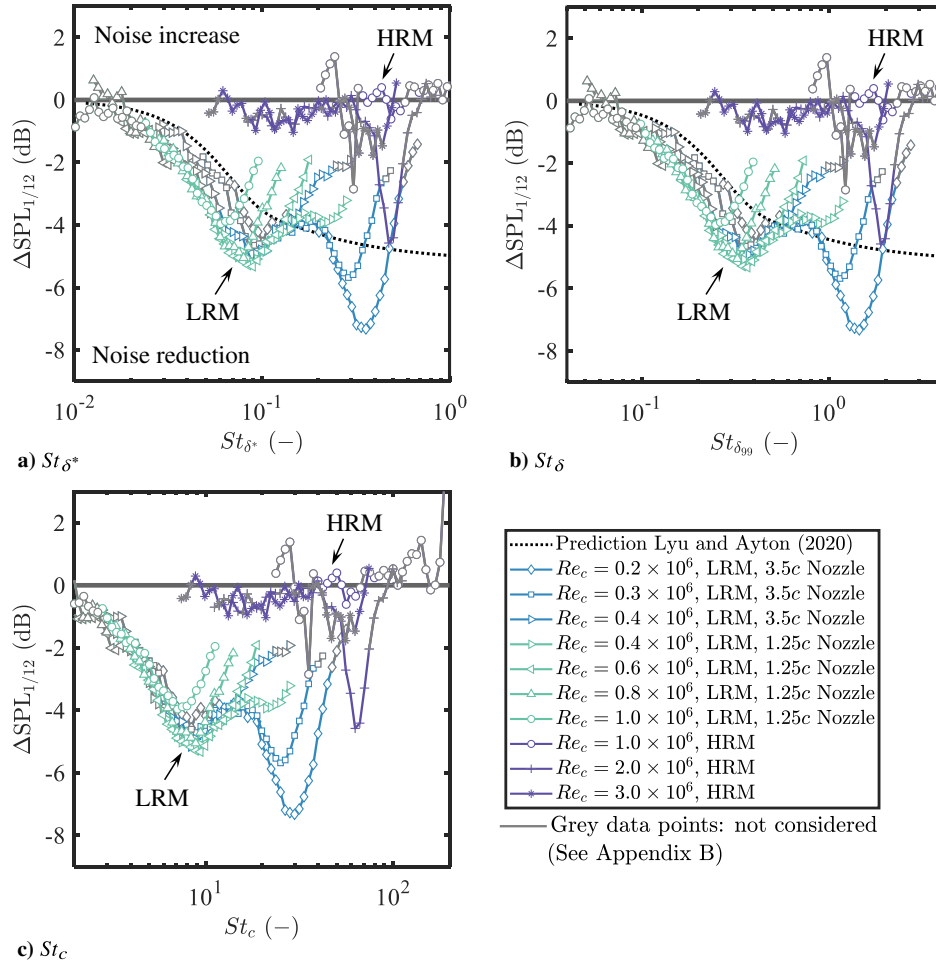


Fig. 29 Scaling of the 1/12 octave band SPL reduction spectra for the LRM and HRM under forced transition condition with by the sawtooth TE serrations with $\varphi = 0$ deg in a wide Re_c range using various length scales for the Strouhal number St .

Table 9 A-weighted scaled acoustic pressure levels based on a fitting of the measurement data with Eq. (10)

TE geometry	Configuration (clean/forced)	$\alpha_{\text{eff.}}$, deg	$L_{A,\text{norm.}}$, dB(A)
Baseline	Clean	0	146.9
Baseline	Forced	0	149.2
Sawtooth	Forced	0	146.9
Iron	Forced	0	146.0
Sawtooth $\varphi = 8$ deg	Forced	0	146.9

Finally, Table 9 summarizes the obtained A-weighted sound pressure levels from the measurements of this work. Data are reduced using a fit of all the speeds and conditions measured using Eq. (10):

$$L_{A,\text{norm.}} = L_A + 50 \log M + 10 \log(\delta_{s.s.}^* + \delta_{p.s.}^*) + 10 \log b \text{ dB(A)} \quad (10)$$

The data provide a comparable measure of the noise levels emitted by the different configurations tested in the experiment, including different angles of attack and serration geometries.

VII. Conclusions

In this paper, aeroacoustic characterization of the NACA 63₃-018 airfoil is presented. The characterization is done in a wide chord-based Reynolds number range of $Re_c = 6 \times 10^4$ to 3×10^6 as well as multiple angles of attack. To achieve this, small and large NACA 63₃-018 airfoil models, denoted as the low- Re_c model and high- Re_c model, respectively, were tested in two wind-tunnel facilities. The

airfoils were tested in the baseline trailing edge configuration with natural and forced transition locations as well as with various TE serrations while the forced transition location was applied.

First, baseline aerodynamic characteristics of the airfoil are examined. For the natural transition configuration, a laminar separation bubble length reduction with increasing Re_c is observed. Additionally, the lift and drag coefficients agree well with the theoretical values and predictions. A consistent trend is observed despite the different model sizes; as Re_c increases, the maximum lift coefficient increases and the drag coefficient reduces.

Next, boundary-layer parameters at the TE are measured. The forced transition location consistently increases the chord-normalized displacement thickness δ^*/c at the TE, which reduces when Re_c increases. Based on the collected boundary-layer data, a fitting equation for the boundary-layer thickness, which is later used to scale acoustic data, at the TE of this airfoil is provided.

For a given Re_c , as the TBL-TE noise dominates, the increase of δ^*/c by the forced transition causes the measured far-field TBL-TE noise level to increase. As the angle of attack increases from 0 deg, the low-frequency content of the TBL-TE noise increases, following the thicker δ^*/c at the suction side of the airfoil.

Scaling of the acoustic data reveals that for a given Re_c and Mach number M the scaled spectra measured from the LRM and the HRM show an overlapping trend. The displacement-thickness-based Strouhal number St_{δ^*} where the peak noise level is found reduces as Re_c increases. This is in agreement with previous literature. The integrated SPLs from both tunnels follow closely the scaling with M^5 .

TBL-TE noise attenuation is found for the case of TE serrations. The results validate the higher noise reduction provided by the iron-shaped serrations over the regular sawtooth serrations observed

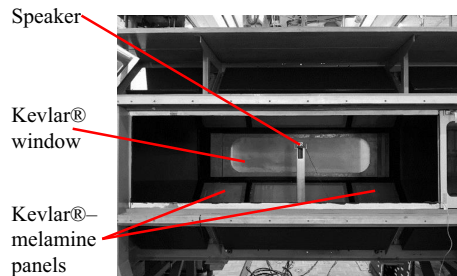
in previous computational studies. The noise increase with increasing angles of attack is found to depend on the airfoil loading; in other words, positive flapped serrations are more sensitive to changes in angle of attack than zero or negative flapped ones. The noise reduction from the serrations is demonstrated to scale with the boundary-layer length scales at the low-frequency range. The present scaling method does not produce accurate matching of the high-frequency cutoff neither of the large-scale results. The latter is believed to be caused by the wide serration scale with respect to the boundary-layer and the wind-tunnel background levels.

The data presented in this paper are publicly available in a repository with the following digital object identifier (DOI): <https://doi.org/10.4121/20940646> and will be further compared to data obtained from other institutions. The ultimate aim is to create an aeroacoustic benchmarking dataset of this 63₃–018 airfoil, which is a representation of generic wind turbine blades.

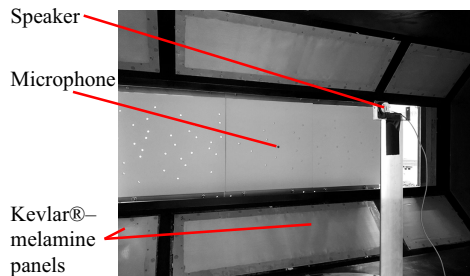
Appendix A: Kevlar® Transmission Loss and Background Noise of LTT

This Appendix describes the characterization of the transmission loss (TL) and background noise properties of the LTT. These properties were measured using a speaker in the empty test section for the TL and with the fully empty test section for the background noise. The following results were presented at the Hybrid Anechoic Wind Tunnel (HAWT) workshop, a session in the AIAA/CEAS Aeroacoustic Conference in 2020 and are provided in this Appendix for completeness.

A Visaton K50 SQ speaker was used to assess the Kevlar® properties. The speaker was positioned at $(X, Y, Z) = (0.5c, 0, 0.12c)$. Synthesized white-noise signal generated in MATLAB® was fed to the speaker. To record the sound signal emitted from the speaker, a LinearX M53 microphone was installed at the center of the microphone array, $(X, Y, Z) = (0.5c, 1.16c, 0)$. Before installation, this microphone was calibrated using a GRAS Type 42AA piston phone. Tests were carried out with and without the stretched Kevlar® panel between the speaker and the microphone to determine the TL.



a) Viewed from outside the test section with the Kevlar® panel



b) Viewed from inside the test section without the Kevlar® panel

Fig. A1 Setup of the speaker and microphone in the empty LTT test section.

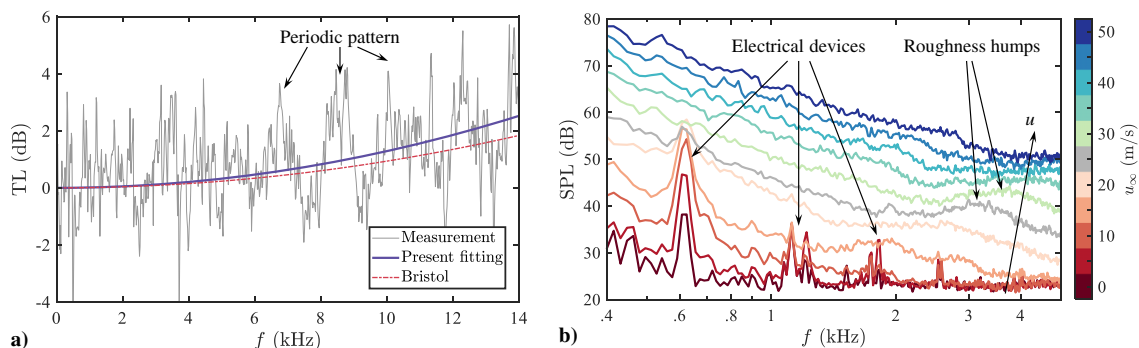


Fig. A2 Acoustic characterization of the empty LTT test section: a) transmission losses (TL) through the Kevlar® sheet and b) background noise SPL spectra measured in the LTT vs flow speeds u_∞ .

Figures A1a and A1b show the setup with and without the Kevlar® panel, respectively.

Data were recorded with a sampling frequency of 51.2 kHz for 2.7 s. Postprocessing in the frequency domain was done by averaging the spectra obtained from fast-Fourier-transformed time domain data snapshots having a length of 0.0625 s, weighted with the Hanning weighting function with 50% data overlap between adjacent time-domain snapshots. The process resulted in a frequency resolution of 16 Hz.

The TL is then calculated following the procedure described by Devenport et al. [32] for the Stability Wind Tunnel at Virginia Polytechnic Institute and State University and Mayer et al. [57] for the Kevlar®-walled test section at the University of Bristol. The latter uses the same Kevlar® cloth type, 49 plain cloth with a weight-per-area ratio of 61 g/m² [33], as the one selected for the LTT test section. The values of TL versus frequency f are shown in Fig. A2a. The periodic pattern of the TL with respect to f is observed in the measured narrowband TL. This is in accordance with previous works [32,58,59]. The following equation is fitted to the data to represent the frequency-dependent TL,

$$TL = K_{TL} \left(\frac{f}{1000} \right)^2 \quad (A1)$$

where a least-squares fitting procedure was used to determine the empirical coefficient K_{TL} . This results in $K_{TL} = 12.9 \times 10^{-3}$, close to the work of Mayer et al. [57] for the Kevlar® section at the University of Bristol ($K_{TL} = 9.4 \times 10^{-3}$). These curves are also shown in Fig. A2a.

The measured narrowband background noise SPL spectra for varying freestream flow speeds u_∞ are shown in Fig. A2b. The levels have been corrected for the TL, and the distance from the center of the test section is assumed to be 1 m (1.11c). Strong tones are captured for $u_\infty \leq 20$ m/s, predominantly at 0.6 kHz. These are attributed to background noise from the motor inverter in the LTT. The same tone is also observed for the measurements of the airfoil at the lowest Re_c case in the LTT (Fig. 20b), indicating that the measured tone is not a self-noise from the airfoil model. For $u_\infty > 20$ m/s, the flow noise

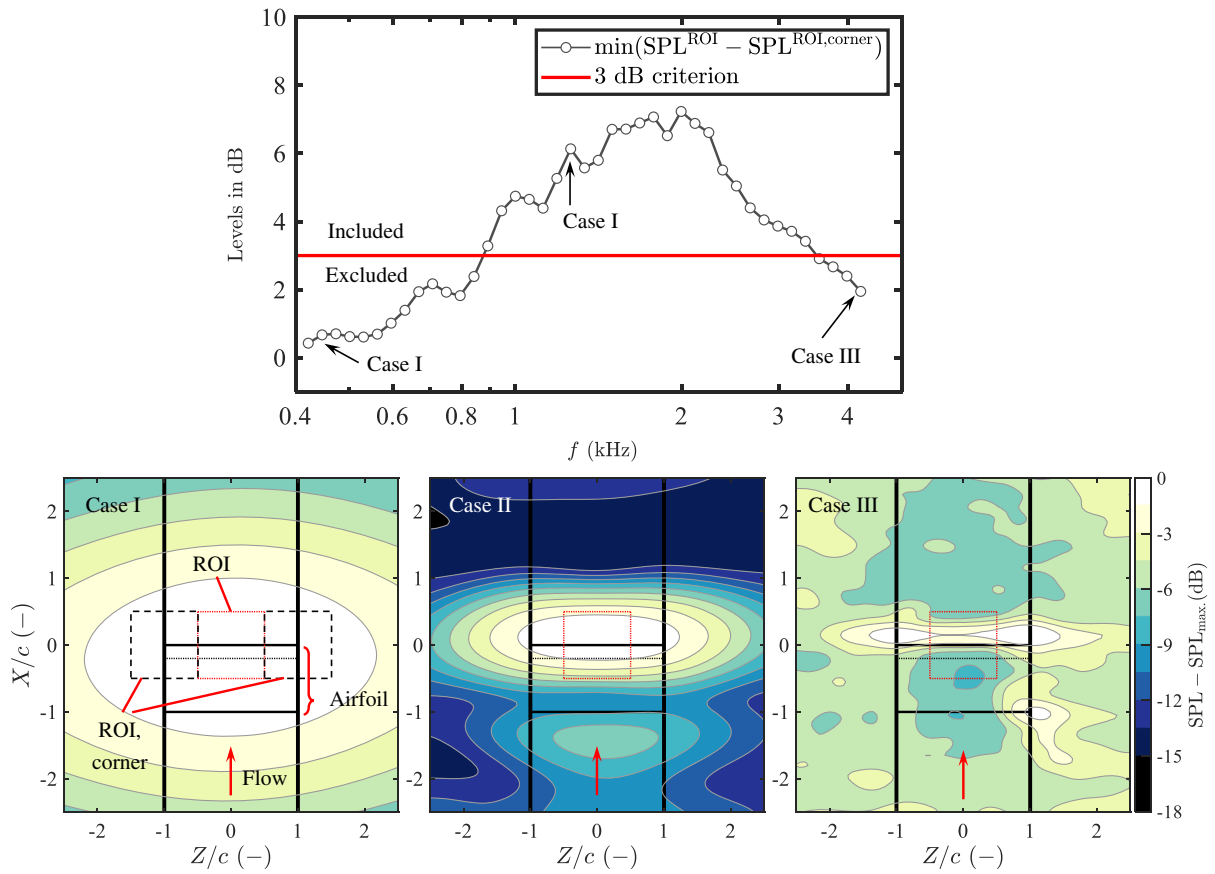


Fig. B1 Truncation of the $SPL_{1/12}$ spectra using the source-map-based criterion set for the A-Tunnel. An exemplary case shown is for the baseline airfoil with forced transition at $Re_c = 0.4 \times 10^6$, $\alpha_{eff} = 0$ deg.

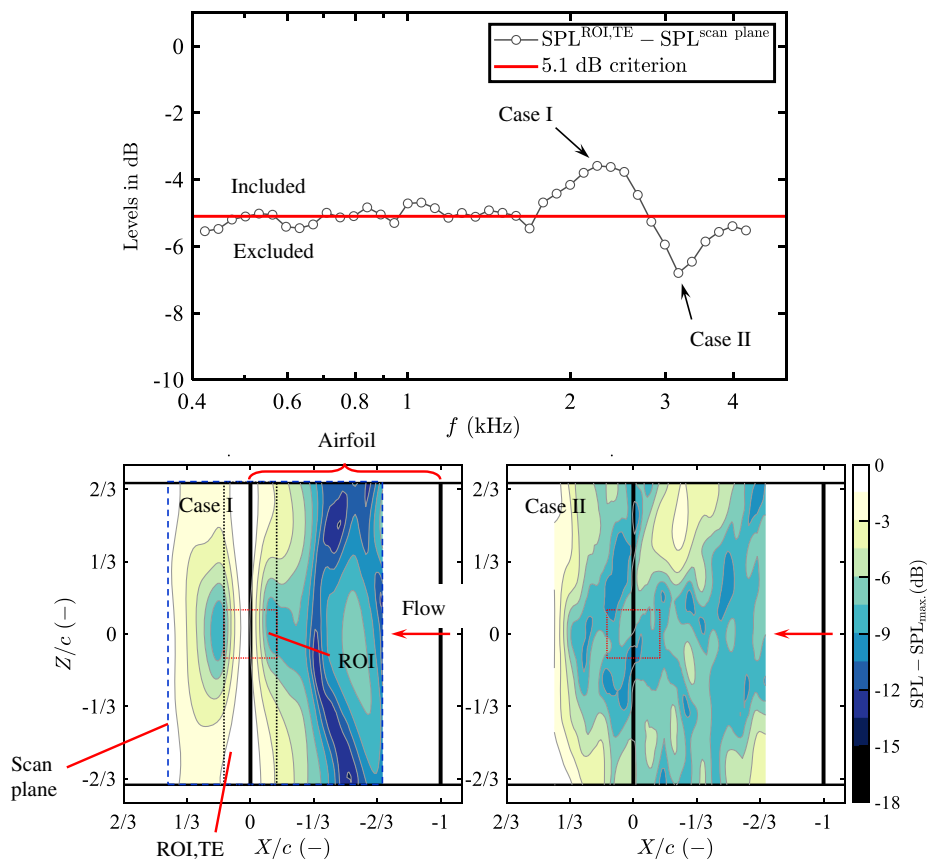


Fig. B2 Truncation of the $SPL_{1/12}$ spectra using the source-map-based criterion set for the LTT. An exemplary case shown is for the baseline airfoil with forced transition at $Re_c = 2 \times 10^6$, $\alpha_{eff} \approx 0$ deg.

dominates, overshadowing the tones, and the background noise levels increase with the increasing u_∞ . Another notable feature of the spectra is the broadband hump, which becomes visible for $u_\infty > 25$ m/s. At $u_\infty = 25$ m/s, the hump reaches its peak at $f \approx 3$ kHz. This part of the spectrum is attributed to the so-called roughness hump, as investigated by Stephens [60] and other studies [61]. This roughness comes from imperfections on the wind-tunnel walls, such as opening gaps between the test section and the LTT circuit.

Appendix B: Source Map Analysis for Scaling Frequency Range Selection

To ensure that parts of the acoustic spectra considered in the scaling studies represent predominantly the TBL-TE noise with minimal contamination from other noise sources in the wind tunnel, criteria are set to either include or exclude the SPL at a given frequency. These criteria are explained in detail in this Appendix.

An analysis is done by examining the acoustic source map per 1/12-octave band frequency f . Different criteria between the A-Tunnel and the LTT are chosen due to the inherent differences in the geometry and acoustic environment of both wind tunnels.

Because of the relatively small airfoil size in the A-Tunnel, the sources at the corners where the airfoil is attached to the side plates often interfere with the trailing-edge noise source. Two additional ROIs are defined adjacent to the main ROI on the left and the right sides. These ROI are called “ROI, corner”. All of the ROI have the same dimension of $c \times c$. These ROI are shown in Fig. B1.

Because ROI, corners cover a span extent that is half as long as the main ROI, a criterion is set such that the minimum difference between the integrated SPL within the main ROI is 3 dB above the corner ROI: $\min(SPL^{\text{ROI}} - SPL^{\text{ROI,corner}}) > 3$ dB.

The aforementioned difference as well as the 3 dB criterion are also shown in Fig. B1 for the LRM under forced transition condition with a baseline TE at $Re_c = 0.4 \times 10^6$ and $\alpha_{\text{eff.}} = 0$ deg. Three source maps belonging to three different f are selected for visualization purposes. Case I at the relatively low f is excluded due to the low resolution. The source at the TE cannot be discerned from those at the side plates. In contrast, case II is included, and the TE sources at the center of the span can be perfectly discerned. Finally, case III at the relatively high f is excluded because the SPLs of the corner sources are more dominant than the SPL within the ROI, possibly affecting the integrated value at the center.

On the other hand, for the LTT, which is inherently not an acoustic wind tunnel, the TE is usually overshadowed by the sources from upstream and downstream, for example, metal meshes and electrical cabinets. To account for this, a ROI covering the same streamwise extent as the main ROI is defined and denoted by “ROI, TE”. The SPL is integrated within this “ROI, TE” and compared to the SPL of the entire scan plane. Considering the streamwise length of ROI,TE compared to the streamwise length of the scan plane, the difference of the integrated SPL between ROI,TE and the scan plane greater than -5.1 dB implies that there is a significant level of noise within ROI, TE compared to the entire scan plane. Therefore, a criterion is set to be $SPL^{\text{ROI,TE}} - SPL^{\text{scanplane}} > -5.1$ dB.

An example is given in Fig. B2 for the HRM under forced transition condition with a baseline TE at $Re_c = 2 \times 10^6$ and

Table C1 Chordwise pressure tap locations on the LRM (the underlined locations mean only on the suction side)

X/c (-)	<u>-0.98</u>	<u>-0.965*</u>	<u>-0.95*</u>	<u>-0.925*</u>	-0.9	-0.875	-0.85	-0.8	-0.7	-0.6	-0.5	-0.4
	-0.325	-0.275	-0.225	<u>-0.175</u>								

Table C2 Chordwise pressure tap locations on the HRM (for both suction side and pressure side)

X/c (-)	-1.0000	-0.9996	-0.9984	-0.9963	-0.9934	-0.9898	-0.9858	-0.9812	-0.9760	-0.9705
	-0.9646	-0.9583	-0.9516	-0.9446*	-0.9373*	-0.9296*	-0.9215	-0.9131	-0.9044	-0.8953
	-0.8859	-0.8762	-0.8635	-0.8478	-0.8291	-0.8074	-0.7826	-0.7548	-0.7239	-0.6899
	-0.6499	-0.6099	-0.5700	-0.5302	-0.4904	-0.4508	-0.4113	-0.3719	-0.3325	-0.2933
	-0.2540	-0.2147	-0.1754	-0.1409	-0.1113	-0.0816	-0.0568	-0.0319	0.0000	

Table C3 Microphone coordinates used in the A-Tunnel, LRM

Microphone No.	X, m	Z, m	Microphone No.	X, m	Z, m	Microphone No.	X, m	Z, m	Microphone No.	X, m	Z, m
1	-0.410	0.030	17	0.640	0.030	33	-0.125	0.120	49	-0.005	-0.180
2	-0.545	-0.030	18	0.745	-0.120	34	-0.230	0.195	50	-0.080	-0.270
3	-0.605	0.120	19	0.730	0.105	35	-0.020	0.315	51	-0.350	-0.150
4	-0.605	-0.135	20	0.880	-0.030	36	-0.410	0.195	52	-0.380	-0.240
5	0.040	0.420	21	0.910	-0.210	37	-0.245	0.330	53	-0.290	-0.345
6	-0.755	0.030	22	0.970	0.105	38	-0.500	0.300	54	-0.605	-0.270
7	-0.695	0.240	23	1.045	-0.105	39	0.460	0.435	55	-0.110	-0.435
8	-0.830	-0.090	24	0.955	0.210	40	-0.185	0.435	56	-0.515	-0.375
9	0.355	0.120	25	0.265	-0.105	41	0.115	0.000	57	0.295	-0.270
10	0.115	0.165	26	0.355	-0.030	42	0.115	-0.135	58	0.025	-0.345
11	0.475	0.195	27	0.325	0.045	43	0.040	0.105	59	0.460	-0.300
12	0.130	0.255	28	0.190	0.105	44	-0.095	0.045	60	0.235	-0.390
13	0.430	0.285	29	0.235	-0.180	45	-0.125	-0.030	61	0.685	-0.270
14	0.715	0.225	30	0.430	-0.105	46	-0.035	-0.105	62	0.490	-0.420
15	0.265	0.360	31	0.475	0.015	47	-0.245	0.015	63	0.715	-0.390
16	0.625	0.345	32	0.580	-0.150	48	-0.200	-0.105	64	0.100	-0.495

Table C4 Microphone coordinates used in the LTT, HRM

Microphone No.	X, m	Z, m	Microphone No.	X, m	Z, m	Microphone No.	X, m	Z, m	Microphone No.	X, m	Z, m
1	0.068	0.014	17	0.417	-0.038	33	-0.328	0.004	49	0.240	0.069
2	0.059	-0.021	18	0.520	0.021	34	-0.271	0.035	50	0.331	-0.006
3	0.124	0.046	19	0.424	-0.089	35	-0.409	0.032	51	0.118	0.128
4	0.183	-0.005	20	0.512	0.098	36	-0.262	0.070	52	0.388	0.059
5	0.097	-0.054	21	0.611	-0.029	37	-0.333	0.103	53	0.315	0.121
6	0.208	-0.079	22	0.365	-0.142	38	-0.266	0.138	54	0.114	0.178
7	0.192	-0.118	23	0.645	0.060	39	-0.396	0.176	55	0.311	0.172
8	0.070	-0.157	24	0.619	-0.079	40	-0.228	0.202	56	0.244	-0.181
9	-0.424	-0.022	25	-0.175	-0.050	41	-0.688	-0.011	57	-0.126	0.000
10	-0.564	-0.034	26	-0.289	-0.030	42	-0.762	0.036	58	-0.147	0.051
11	-0.547	0.045	27	-0.094	-0.078	43	-0.704	-0.076	59	-0.013	0.042
12	-0.584	0.083	28	-0.299	-0.065	44	-0.779	0.091	60	-0.037	-0.046
13	-0.529	-0.100	29	-0.376	-0.097	45	-0.858	-0.037	61	-0.051	0.076
14	-0.523	0.131	30	-0.181	-0.142	46	-0.719	0.138	62	-0.022	0.113
15	-0.376	-0.152	31	-0.110	-0.188	47	-0.769	-0.123	63	-0.071	-0.115
16	-0.593	-0.147	32	-0.304	-0.199	48	-0.933	0.010	64	-0.097	0.165

$\alpha_{\text{eff}} \approx 0$ deg. For case I, which is included in the scaling, the TE region is clearly visible. For case II, spurious sound sources are seen in the map without a clear view of the TE. The latter is therefore excluded.

Appendix C: Supplementary Coordinates

A. Pressure Tap Coordinates

The chordwise locations of the pressure taps on the LRM and HRM are provided in Tables C1 and C2, respectively. The superscript * indicates the pressure taps that may be blocked or interfered by the tripping strip.

B. Microphone Array Coordinates

The microphone array coordinates used in the A-Tunnel (LRM tests) and LTT (HRM tests) are provided in Tables C3 and C4, respectively. The A-Tunnel array was installed at $Y = -1$ m ($-5c$), while the LTT array was installed at $Y = 1.044$ m ($1.16c$).

Acknowledgments

The authors would like to acknowledge Michaela Herr from the German Aerospace Center (DLR) and Andreas Fischer from the Technical University of Denmark (DTU) for their helpful input regarding the airfoil design. Salil Luesutthiviboon is funded by the Netherlands Organization for Scientific Research (project number 15452). Lourenco Tercio Lima Pereira is funded by the European Union's Horizon 2020 research and innovation program (grant agreement number 722401).

References

- [1] Howe, M. S., "A Review of the Theory of Trailing Edge Noise," *Journal of Sound and Vibration*, Vol. 61, No. 3, 1978, pp. 437–465. [https://doi.org/10.1016/0022-460X\(78\)90391-7](https://doi.org/10.1016/0022-460X(78)90391-7)
- [2] Lee, S., Ayton, L., Bertagnolio, F., Moreau, S., Chong, T. P., and Joseph, P., "Turbulent Boundary Layer Trailing-Edge Noise: Theory, Computation, Experiment, and Application," *Progress in Aerospace Sciences*, Vol. 126, Oct. 2021, p. 100737. <https://doi.org/10.1016/j.paerosci.2021.100737>
- [3] Oerlemans, S., Sijtsma, P., and López, B. M., "Location and Quantification of Noise Sources on a Wind Turbine," *Journal of Sound and Vibration*, Vol. 299, Nos. 4–5, 2007, pp. 869–883. <https://doi.org/10.1016/j.jsv.2006.07.032>
- [4] Dobrzynski, W., "Almost 40 Years of Airframe Noise Research: What Did We Achieve?" *Journal of Aircraft*, Vol. 47, No. 2, 2010, pp. 353–367. <https://doi.org/10.2514/1.44457>
- [5] Amiet, R. K., "Noise Due to Turbulent Flow Past a Trailing Edge," *Journal of Sound and Vibration*, Vol. 47, No. 3, 1976, pp. 387–393. [https://doi.org/10.1016/0022-460X\(76\)90948-2](https://doi.org/10.1016/0022-460X(76)90948-2)
- [6] Brooks, T. F., Pope, D. S., and Marcolini, M. A., "Airfoil Self-Noise and Prediction," NASA-RP-1218, 1989.
- [7] Ferret Gasch, O., Oerlemans, S., Bertagnolio, F., Fischer, A., Arnold, B., Lutz, T., Fassmann, B. W., and Herr, M., "Trailing Edge Noise Prediction of Wind Turbine Airfoils: A Benchmark Exercise," *25th AIAA/CEAS Aeroacoustics Conference*, AIAA Paper 2019-2675, 2019. <https://doi.org/10.2514/6.2019-2675>
- [8] Herr, M., and Kamruzzaman, M., "Benchmarking of Trailing-Edge Noise Computations—Outcome of the BANC-II Workshop," *19th AIAA/CEAS Aeroacoustics Conference*, AIAA Paper 2013-2123, 2013. <https://doi.org/10.2514/6.2013-2123>
- [9] Herr, M., Ewert, R., Rautmann, C., Kamruzzaman, M., Bekiropoulos, D., Arina, R., Iob, A., Batten, P., Chakravarthy, S., and Bertagnolio, F., "Broadband Trailing-Edge Noise Predictions—Overview of BANC-III Results," *21st AIAA/CEAS Aeroacoustics Conference*, AIAA Paper 2015-2847, 2015. <https://doi.org/10.2514/6.2015-2847>
- [10] Allen, C. S., Blake, W. K., Dougherty, R. P., Lynch, D., Soderman, P. T., and Underbrink, J. R., *Aeroacoustic Measurements*, Springer, Berlin, Heidelberg, 2002.
- [11] Howe, M., "Aerodynamic Noise of a Serrated Trailing Edge," *Journal of Fluids and Structures*, Vol. 5, No. 1, 1991, pp. 33–45. [https://doi.org/10.1016/0889-9746\(91\)80010-B](https://doi.org/10.1016/0889-9746(91)80010-B)
- [12] Gruber, M., Joseph, P., and Chong, T., "On the Mechanisms of Serrated Airfoil Trailing Edge Noise Reduction," *17th AIAA/CEAS Aeroacoustics Conference*, AIAA Paper 2011-2781, 2011. <https://doi.org/10.2514/6.2011-2781>
- [13] Lyu, B., and Ayton, L. J., "Rapid Noise Prediction Models for Serrated Leading and Trailing Edges," *Journal of Sound and Vibration*, Vol. 469, March 2020, Paper 115136. <https://doi.org/10.1016/j.jsv.2019.115136>
- [14] Avallone, F., Pröbsting, S., and Ragni, D., "Three-Dimensional Flow Field over a Trailing-Edge Serration and Implications on Broadband Noise," *Physics of Fluids*, Vol. 28, No. 11, 2016, Paper 117101. <https://doi.org/10.1063/1.4966633>
- [15] Zhou, P., Liu, Q., Zhong, S., Fang, Y., and Zhang, X., "A Study of the Effect of Serration Shape and Flexibility on Trailing Edge Noise," *Physics of Fluids*, Vol. 32, No. 12, 2020, Paper 127114. <https://doi.org/10.1063/5.0032774>
- [16] Oerlemans, S., Fisher, M., Maeder, T., and Kögler, K., "Reduction of Wind Turbine Noise Using Optimized Airfoils and Trailing-Edge Serrations," *AIAA Journal*, Vol. 47, No. 6, 2009, pp. 1470–1481. <https://doi.org/10.2514/1.38888>
- [17] Oerlemans, S., "Reduction of Wind Turbine Noise Using Blade Trailing Edge Devices," *22nd AIAA/CEAS Aeroacoustics Conference*, AIAA Paper 2016-3018, 2016. <https://doi.org/10.2514/6.2016-3018>
- [18] Wang, Y., Zhao, K., Lu, X.-Y., Song, Y.-B., and Bennett, G. J., "Bio-inspired Aerodynamic Noise Control: A Bibliographic Review," *Applied Sciences*, Vol. 9, No. 11, 2019, p. 2224. <https://doi.org/10.3390/app9112224>

- [19] Abbott, I. H., and von Doenhoff, A. E., *Theory of Wing Sections: Including a Summary of Airfoil Data*, General Publishing Company, Ltd., Toronto, Ontario, 2012.
- [20] Timmer, W., "An Overview of NACA 6-Digit Airfoil Series Characteristics with Reference to Airfoils for Large Wind Turbine Blades," *47th AIAA Aerospace Sciences Meeting and Exhibit*, AIAA Paper 2009-268, 2009. <https://doi.org/10.2514/6.2009-268>
- [21] Timmer, W., and van Rooij, R., "Summary of the Delft University Wind Turbine Dedicated Airfoils," *41st AIAA Aerospace Sciences Meeting and Exhibit*, AIAA Paper 2003-352, 2003. <https://doi.org/10.2514/6.2003-352>
- [22] Avallone, F., der Velden, W. C. P. V., and Ragni, D., "Benefits of Curved Serrations on Broadband Trailing-Edge Noise Reduction," *Journal of Sound and Vibration*, Vol. 400, July 2017, pp. 167–177. <https://doi.org/10.1016/j.jsv.2017.04.007>
- [23] Borgoltz, A., Intaratep, N., and Devenport, W. J., "Aerodynamic Effects of Boundary Layer Trip Strips on the Flow over a NACA63018 Airfoil," Virginia Polytechnic Inst. and State Univ., Blacksburg, VA, 2019, http://www.dept.aoe.vt.edu/~aborgolt/aoe3054/manual/exp7/AOE3054_2018_Exp7.pdf.
- [24] Verges i Plaza, G., Fischer, A., Lylloff, O., Bak, C., Olsen, A. S., Bertagnolio, F., Luesutthiviboon, S., Lima Pereira, L. T., Ragni, D., Avallone, F., Suryadi, A., and Herr, M., "Benchmarking of the NACA 633-018 Trailing-Edge Noise in a Broad Reynolds Number Range as Part of the IEA Task 39," *28th AIAA/CEAS Aeroacoustics 2022 Conference*, AIAA Paper 2022-2981, June 2022. <https://doi.org/10.2514/6.2022-2981>
- [25] Ye, Q., Avallone, F., Ragni, D., Choudhari, M., and Casalino, D., "Effect of Surface Roughness Geometry on Boundary-Layer Transition and Far-Field Noise," *AIAA Journal*, Vol. 59, No. 7, 2021, pp. 2396–2408. <https://doi.org/10.2514/1.j059335>
- [26] Braslow, A. L., Hicks, R. M., and Harris, R. V., "Use of Grit-Type Boundary-Layer-Transition Trips on Wind-Tunnel Models," NASA-TN-D-3579, 1966, <https://ntrs.nasa.gov/citations/19660026829>.
- [27] Arce León, C., Merino-Martínez, R., Ragni, D., Avallone, F., Scarano, F., Pröbsting, S., Snellen, M., Simons, D. G., and Madsen, J., "Effect of Trailing Edge Serration-Flow Misalignment on Airfoil Noise Emissions," *Journal of Sound and Vibration*, Vol. 405, Sept. 2017, pp. 19–33. <https://doi.org/10.1016/j.jsv.2017.05.035>
- [28] "ISO 3382-2:2008 Acoustics—Measurement of Room Acoustic Parameters—Part 2: Reverberation Time in Ordinary Rooms," 2008, <https://www.iso.org/standard/36201.html>.
- [29] Merino-Martínez, R., Carpio, A. R., Pereira, L. T. L., van Herk, S., Avallone, F., Ragni, D., and Kotsonis, M., "Aeroacoustic Design and Characterization of the 3D-printed, Open-Jet, Anechoic Wind Tunnel of Delft University of Technology," *Applied Acoustics*, Vol. 170, Dec. 20 20, Paper 107504. <https://doi.org/10.1016/j.apacoust.2020.107504>
- [30] Brooks, T. F., Marcolini, M. A., and Pope, D. S., "Airfoil Trailing Edge Flow Measurements and Comparisons with Theory, Incorporating Open Wind Tunnel Corrections," AIAA Paper 1984-2266, 1984. <https://doi.org/10.2514/6.1984-2266>
- [31] Timmer, W. A., "Two-Dimensional Low-Reynolds Number Wind Tunnel Results for Airfoil NACA 0018," *Wind Engineering*, Vol. 32, No. 6, 2008, pp. 525–537. <https://doi.org/10.1260/030952408787548848>
- [32] Devenport, W. J., Burdisso, R. A., Borgoltz, A., Ravetta, P. A., Barone, M. F., Brown, K. A., and Morton, M. A., "The Kevlar-Walled Anechoic Wind Tunnel," *Journal of Sound and Vibration*, Vol. 332, No. 17, 2013, pp. 3971–3991. <https://doi.org/10.1016/j.jsv.2013.02.043>
- [33] ECC, Technisches Datenblatt, Style 120, Engineered Cramer Composites, July 2009, http://www.ezentrumbilder.de/rg/pdf/td_de_ECC_Style120_D.pdf.
- [34] Devenport, W., Burdisso, R., Borgoltz, A., Ravetta, P., and Barone, M., "Aerodynamic and Acoustic Corrections for a Kevlar-Walled Anechoic Wind Tunnel," *16th AIAA/CEAS Aeroacoustics Conference*, AIAA Paper 2010-3749, 2010. <https://doi.org/10.2514/6.2010-3749>
- [35] Luesutthiviboon, S., Malgoezar, A., Snellen, M., Sijtsma, P., and Simons, D., "Improving Source Discrimination Performance by Using an Optimized Acoustic Array and Adaptive High-Resolution CLEAN-SC Beamforming," *7th Berlin Beamforming Conference*, Paper BeBeC-2018-D07, 2018, pp. 1–26.
- [36] Sarraji, E., Herold, G., Sijtsma, P., Martínez, R. M., Geyer, T. F., Bahr, C. J., Porteous, R., Moreau, D., and Doolan, C. J., "A Microphone Array Method Benchmarking Exercise Using Synthesized Input Data," *23rd AIAA/CEAS Aeroacoustics Conference*, AIAA Paper 2017-3719, 2017. <https://doi.org/10.2514/6.2017-3719>
- [37] Merino-Martínez, R., Sijtsma, P., Carpio, A. R., Zamponi, R., Luesutthiviboon, S., Malgoezar, A. M., Snellen, M., Schram, C., and Simons, D. G., "Integration Methods for Distributed Sound Sources," *International Journal of Aeroacoustics*, Vol. 18, Nos. 4–5, 2019, pp. 444–469. <https://doi.org/10.1177/1475472x19852945>
- [38] Johnson, D. H., and Dudgeon, D. E., *Array Signal Processing, Concepts and Techniques*, Prentice-Hall, Upper Saddle River, NJ, 1993.
- [39] van Veen, B., and Buckley, K., "Beamforming: A Versatile Approach to Spatial Filtering," *IEEE ASSP Magazine*, Vol. 5, No. 2, 1988, pp. 4–24. <https://doi.org/10.1109/53.665>
- [40] Sijtsma, P., "Phased Array Beamforming Applied to Wind Tunnel and Fly-Over Tests," Soc. of Automotive Engineers TP 2010-36-0514, Oct. 2010, pp. 17–19. <https://doi.org/10.4271/2010-36-0514>
- [41] Russo, G. P., *Aerodynamic Measurements: From Physical Principles to Turnkey Instrumentation*, Woodhead Publishing in Mechanical Engineering, Woodhead Publishing Limited, Cambridge, U.K., 2011, p. 236.
- [42] Barlow, J. B., Rae, W. H., and Pope, A., *Low-Speed Wind Tunnel Testing*, Wiley, Hoboken, NJ, 1999, p. 177.
- [43] Houghton, E. L., and Carpenter, P. W., *Aerodynamics for Engineering Students*, Elsevier, London, 2003, p. 470.
- [44] Drela, M., "XFOIL: An Analysis and Design System for Low Reynolds Number Airfoils," *Lecture Notes in Engineering*, Springer-Verlag, Berlin, 1989, pp. 1–12. https://doi.org/10.1007/978-3-642-84010-4_1
- [45] Moreau, S., Henner, M., Iaccarino, G., Wang, M., and Roger, M., "Analysis of Flow Conditions in Freejet Experiments for Studying Airfoil Self-Noise," *AIAA Journal*, Vol. 41, No. 10, 2003, pp. 1895–1905. <https://doi.org/10.2514/2.1905>
- [46] Garner, H. C., Rogers, E. W. E., Acum, W. E. A., and Maskell, E. C., "Subsonic Wind Tunnel Wall Corrections," AGARD Rept. 1996, <https://apps.dtic.mil/sti/citations/AD0657092>.
- [47] Bruun, H. H., *Hot Wire Anemometry: Principles and Signal Analysis*, Oxford Univ. Press, Oxford, England, U.K., 1995, <http://catdir.loc.gov/catdir/enhancements/fy0605/94046236-t.html>.
- [48] Raffel, M., Willert, C. E., Scarano, F., Kähler, C. J., Wereley, S. T., and Kompenhans, J., *Particle Image Velocimetry*, Springer International Publishing AG, Cham, Switzerland, 2018. <https://doi.org/10.1007/978-3-319-68852-7>
- [49] Spalart, P. R., and Watmuff, J. H., "Experimental and Numerical Study of a Turbulent Boundary Layer with Pressure Gradients," *Journal of Fluid Mechanics*, Vol. 249, No. 1, 1993, p. 337. <https://doi.org/10.1017/S002211209300120X>
- [50] Clauser, F. H., "The Turbulent Boundary Layer," *Advances in Applied Mechanics*, Vol. 4, No. C, 1956, pp. 1–51. [https://doi.org/10.1016/S0065-2156\(08\)70370-3](https://doi.org/10.1016/S0065-2156(08)70370-3)
- [51] Coles, D., "The Law of the Wake in the Turbulent Boundary Layer," *Journal of Fluid Mechanics*, Vol. 1, No. 2, 1956, pp. 191–226. <https://doi.org/10.1017/S0022112056000135>
- [52] Schlichting, H., *Boundary-Layer Theory*, McGraw-Hill, New York, 1979, pp. 29–50.
- [53] Zhu, W. J., Shen, W. Z., Sørensen, J. N., and Leloudas, G., "Improvement of Airfoil Trailing Edge Bluntness Noise Model," *Advances in Mechanical Engineering*, Vol. 8, No. 2, 2016, p. 1687814016629343. <https://doi.org/10.1177/1687814016629343>
- [54] Ffowcs-Williams, J. E., and Hall, L. H., "Aerodynamic Sound Generation by Turbulent Flow in the Vicinity of a Scattering Half Plane," *Journal of Fluid Mechanics*, Vol. 40, No. 4, 1970, pp. 657–670. <https://doi.org/10.1017/S0022112070000368>
- [55] Moreau, D. J., and Doolan, C. J., "Noise-Reduction Mechanism of a Flat-Plate Serrated Trailing Edge," *AIAA Journal*, Vol. 51, No. 10, 2013, pp. 2513–2522. <https://doi.org/10.2514/1.j052436>
- [56] Hwang, Y. F., Bonness, W. K., and Hambric, S. A., "Comparison of Semi-Empirical Models for Turbulent Boundary Layer Wall Pressure Spectra," *Journal of Sound and Vibration*, Vol. 319, Nos. 1–2, 2009, pp. 199–217. <https://doi.org/10.1016/j.jsv.2008.06.002>
- [57] Mayer, Y. D., Jawahar, H. K., Szoke, M., Ali, S. A. S., and Azarpeyvand, M., "Design and Performance of an Aeroacoustic Wind Tunnel Facility at the University of Bristol," *Applied Acoustics*, Vol. 155, Dec. 2019, pp. 358–370. <https://doi.org/10.1016/j.apacoust.2019.06.005>

- [58] Li, L., Liu, P., Guo, H., Hou, Y., Geng, X., and Wang, J., "Aeroacoustic Measurement of 30P30N High-Lift Configuration in the Test Section with Kevlar Cloth and Perforated Plate," *Aerospace Science and Technology*, Vol. 70, Nov. 2017, pp. 590–599.
<https://doi.org/10.1016/j.ast.2017.08.039>
- [59] Jaeger, S., Horne, W., and Allen, C., "Effect of Surface Treatment on Array Microphone Self-Noise," *6th AIAA/CEAS Aeroacoustics Conference*, AIAA Paper 2000-1937, 2000.
<https://doi.org/10.2514/6.2000-1937>
- [60] Stephens, D., "The Acoustic Environment of the NASA Glenn 9- by 15-Foot Low-Speed Wind Tunnel," *21st AIAA/CEAS Aeroacoustics Conference*, AIAA Paper 2015-2684, 2015.
<https://doi.org/10.2514/6.2015-2684>
- [61] Alexander, W. N., "Sound from Rough Wall Boundary Layer," 2011, <https://vtechworks.lib.vt.edu/handle/10919/29246>.

X. Zhang
Associate Editor